

1  
2 **Post-infectious inflammatory disease in MIS-C features elevated**  
3 **cytotoxicity signatures and autoreactivity that correlates with severity**  
4  
5  
6

7 Anjali Ramaswamy<sup>1‡</sup>, Nina N. Brodsky<sup>1,2‡</sup>, Tomokazu S. Sumida<sup>1,3‡</sup>, Michela Comi<sup>1,3</sup>, Hiromitsu  
8 Asashima<sup>1,3</sup>, Kenneth B. Hoehn<sup>4</sup>, Ningshan Li<sup>5</sup>, Yunqing Liu<sup>5</sup>, Aagam Shah<sup>12,13</sup>, Neal G.  
9 Ravindra<sup>12,13</sup>, Jason Bishaj<sup>12,13</sup>, Alamzeb Khan<sup>2</sup>, William Lau<sup>8,9</sup>, Brian Sellers<sup>8</sup>, Neha Bansal<sup>8,9</sup>,  
10 Pamela Guerrerio<sup>10</sup>, Avraham Unterman<sup>7</sup>, Victoria Habet<sup>2</sup>, Andrew J. Rice<sup>1</sup>, Jason Catanzaro<sup>2</sup>,  
11 Harsha Chandnani<sup>6</sup>, Merrick Lopez<sup>6</sup>, Naftali Kaminski<sup>7</sup>, Charles S. Dela Cruz<sup>7</sup>, John S. Tsang<sup>8,9</sup>,  
12 Zuoheng Wang<sup>5</sup>, Xiting Yan<sup>5,7</sup>, Steven H. Kleinstein<sup>4,11</sup>, David van Dijk<sup>12,13</sup>, Richard W. Pierce<sup>2</sup>,  
13 David A. Hafler<sup>1,3</sup>, and Carrie L. Lucas<sup>1\*</sup>  
14

15  
16 <sup>1</sup>Department of Immunobiology, Yale University School of Medicine, New Haven, CT.

17 <sup>2</sup>Department of Pediatrics, Yale University School of Medicine, New Haven, CT.

18 <sup>3</sup>Department of Neurology, Yale University School of Medicine, New Haven, CT.

19 <sup>4</sup>Department of Pathology, Yale University School of Medicine, New Haven, CT.

20 <sup>5</sup>Department of Biostatistics, Yale School of Public Health, New Haven, CT.

21 <sup>6</sup>Department of Pediatrics, Loma Linda School of Medicine, Loma Linda, CA.

22 <sup>7</sup>Section of Pulmonary, Critical Care and Sleep Medicine, Yale University School of Medicine, New,  
23 Haven, CT.

24 <sup>8</sup>NIH Center for Human Immunology (CHI), NIH, Bethesda, MD.

25 <sup>9</sup>Multiscale Systems Biology Section, Laboratory of Immune System Biology, NIAID, NIH.

26 <sup>10</sup>Food Allergy Research Section, Laboratory of Allergic Diseases, NIAID, NIH.

27 <sup>11</sup>Interdepartmental Program in Computational Biology and Bioinformatics, Yale University, New  
28 Haven, CT.

29 <sup>12</sup>Department of Internal Medicine (Cardiology), Yale University School of Medicine, New Haven, CT.

30 <sup>13</sup>Department of Computer Science, Yale University, New Haven, CT.  
31

32 ‡Equal contributors

33 \*Correspondence: [Carrie.Lucas@yale.edu](mailto:Carrie.Lucas@yale.edu); 203-785-7158  
34

35 **Word count:** 3308

36 **References:** 49

37 **SUMMARY**

38 Multisystem inflammatory syndrome in children (MIS-C) is a life-threatening post-  
39 infectious complication occurring unpredictably weeks after mild or asymptomatic SARS-CoV2  
40 infection in otherwise healthy children. Here, we define immune abnormalities in MIS-C compared  
41 to adult COVID-19 and pediatric/adult healthy controls using single-cell RNA sequencing, antigen  
42 receptor repertoire analysis, unbiased serum proteomics, and *in vitro* assays. Despite no  
43 evidence of active infection, we uncover elevated S100A-family alarmins in myeloid cells and  
44 marked enrichment of serum proteins that map to myeloid cells and pathways including cytokines,  
45 complement/coagulation, and fluid shear stress in MIS-C patients. Moreover, NK and CD8 T cell  
46 cytotoxicity genes are elevated, and plasmablasts harboring IgG1 and IgG3 are expanded.  
47 Consistently, we detect elevated binding of serum IgG from severe MIS-C patients to activated  
48 human cardiac microvascular endothelial cells in culture. Thus, we define immunopathology  
49 features of MIS-C with implications for predicting and managing this SARS-CoV2-induced critical  
50 illness in children.

51

52 **Key words:** SARS-CoV2, MIS-C, pediatric, inflammation

## 53 INTRODUCTION

54 Pediatric patients are largely spared of severe respiratory pathology associated with  
55 SARS-CoV2 infection; however, recent data has drawn attention to a severe and delayed post-  
56 SARS-CoV2 inflammatory response in children. This ‘multisystem inflammatory syndrome in  
57 children’ (MIS-C) presents in youth who had a mild or asymptomatic SARS-CoV2 infection roughly  
58 4-6 weeks prior<sup>1-9</sup>. Symptoms in MIS-C patients vary and involve a systemic cytokine storm with  
59 fever, gastrointestinal, cardiac, vascular, hematologic, mucocutaneous, neurologic, and  
60 respiratory pathology, leading to critical illness with distributive/cardiogenic shock in up to 80% of  
61 patients and a 2% mortality rate<sup>1</sup>. Most patients with this syndrome are previously healthy with no  
62 co-morbidities and recover with supportive care and immune suppressive therapy. Further  
63 understanding the pathophysiology of this disease is imperative to predict, prevent, and optimally  
64 treat MIS-C in children exposed to SARS-CoV2.

65 Initial reports compared MIS-C with Kawasaki Disease (KD) because of the common  
66 presentation with fever, rash, and coronary aneurysms<sup>2,3,5,7,8</sup>. However, MIS-C predominantly  
67 affects older children with an increased prevalence among Black and Hispanic/Latino populations,  
68 whereas KD affects very young children with higher occurrence in East Asian populations.  
69 Moreover, MIS-C has distinct gastrointestinal symptoms, leukopenia, and high B-type natriuretic  
70 peptide, troponin, ferritin, and C-reactive protein, and it more frequently leads to shock<sup>2,10</sup>. Acute  
71 MIS-C has been further characterized by high systemic inflammatory cytokines such as  
72 interleukin-1 $\beta$  (IL-1 $\beta$ ), IL-6, IL-8, IL-10, IL-17, IFN- $\gamma$ <sup>11</sup>. Also reported is a cytokine profile indicative  
73 of NK, T cell, monocyte and neutrophil recruitment, mucosal immunity, and immune cell negative  
74 feedback<sup>12</sup>. Analysis of peripheral blood mononuclear cells (PBMCs) from MIS-C patients has  
75 revealed CD4, CD8,  $\gamma\delta$  T cell and B cell lymphopenia, with high HLA-DR expression on  $\gamma\delta$  and  
76 CCR7+ CD4 T cells, elevated CD64 expression on neutrophils and monocytes, and low HLA-DR  
77 and CD86 on monocytes and dendritic cells<sup>11</sup>. Neutralizing anti-SARS-CoV2 antibody responses

78 in MIS-C closely resemble convalescent COVID-19, and recent studies also report higher  
79 complement C5b9 in serum and misshapen red blood cells, which are consistent with endothelial  
80 cell activation and clinical findings of distributive and cardiogenic shock<sup>12-14</sup>. Using panels of  
81 human antigens to screen for autoantibodies, acute MIS-C patients were described to have  
82 increased antibody binding to antigens associated with endothelium and heart development and  
83 other common autoimmunity targets as compared to healthy controls<sup>12,13</sup>. As such, one of the  
84 dominant hypotheses to explain the immunopathology of MIS-C has been autoimmunity triggered  
85 by self-reactive antibodies produced in response to SARS-CoV2, as reported in KD where the  
86 presumed infectious trigger is often unknown<sup>15-18</sup>. This hypothesis, however, has not yet been  
87 directly tested.

88 Here, we report 15 cases of MIS-C and elucidate correlates of immunopathology using  
89 single-cell RNA sequencing with antigen receptor repertoire analysis, serum proteomics, and  
90 functional studies in a subset of acute and recovered MIS-C patients compared to healthy  
91 pediatric donors, adult COVID-19 patients, and healthy adults. We find innate and adaptive  
92 immune triggering during acute MIS-C that features elevated innate alarmins, acute inflammatory  
93 serum proteins, heightened cytotoxicity signatures, and expansion of IgG plasmablasts that  
94 correlate with serum antibody binding to cultured activated human cardiac microvascular  
95 endothelial cells in severe MIS-C.

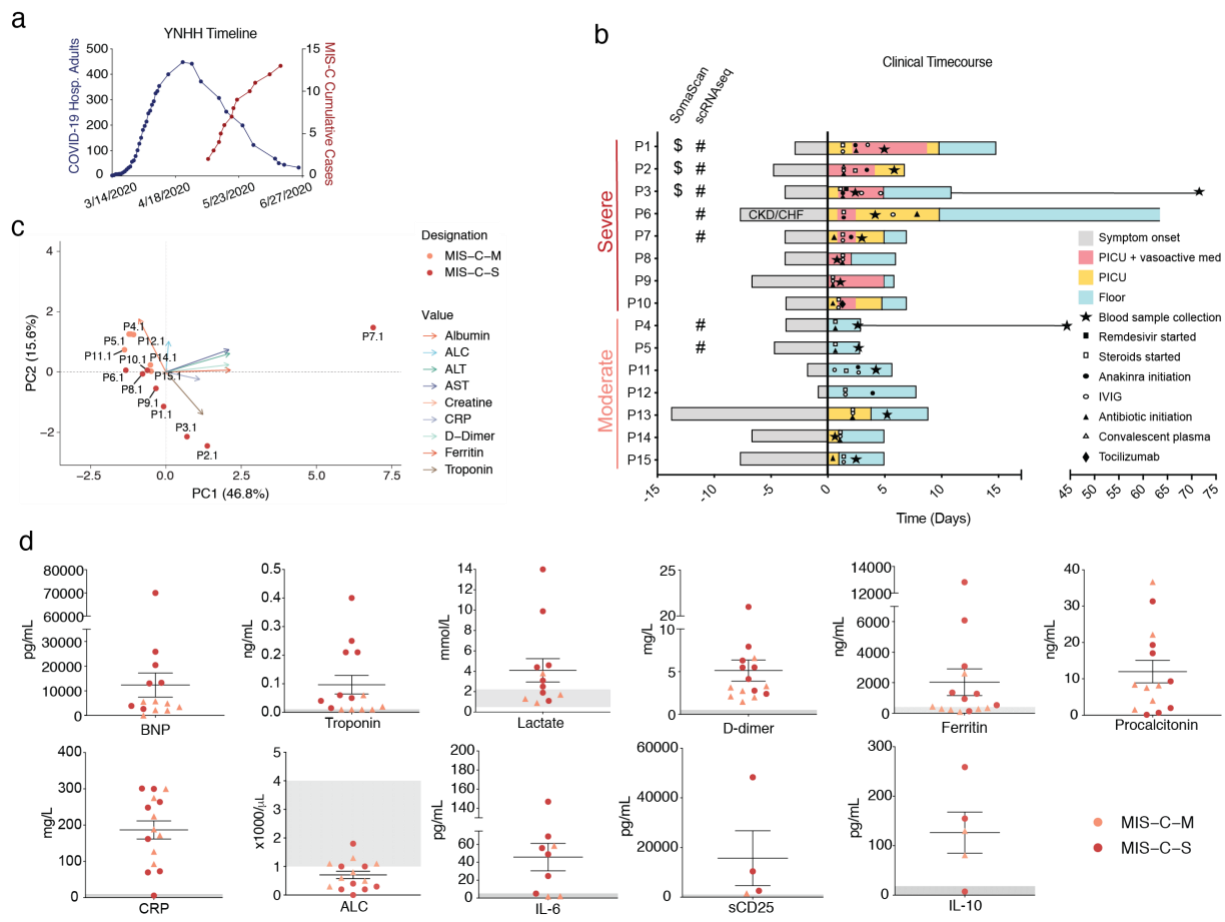
96

## 97 **RESULTS**

### 98 *Clinical characteristics distinguish moderate and severe MIS-C*

99 Our clinical cohort includes 15 MIS-C patients, divided into severe and moderate groups  
100 based on clinical criteria (**Table S1**). Severe patients were critically ill, with cardiac and/or  
101 pulmonary failure (requiring vasoactive medication and/or significant respiratory support with  
102 positive pressure or mechanical ventilation), although not due to primary hypoxia. Most patients

103 presented to care 4-6 weeks after peak adult COVID-19 hospitalizations (**Figure 1a**). Although a  
104 minority (6/15) of patients tested positive for SARS-CoV2 virus near the limit of detection during  
105 hospitalization, all of the patients had positive SARS-CoV2 serology. A majority of subjects  
106 presented with fever, gastrointestinal symptoms, and rash (**Figure S1a**). Two patients developed  
107 coronary aneurysms (**Figure S1a**), and most of the severe patients had depressed left ventricular  
108 heart function. All children received steroids, with a majority also receiving intravenous  
109 immunoglobulin (IVIG), and aspirin. Most severe patients also received vasoactive medications  
110 (epinephrine, norepinephrine, vasopressin, dopamine, and/or milrinone) and anakinra, an IL-1  
111 receptor antagonist, along with heparin (enoxaparin) for anticoagulation and a course of  
112 antibiotics prior to negative culture results (**Figure 1b**). Notably, PCA of clinical lab values  
113 separated severe and moderate MIS-C patients (**Figures 1c** and **S1b-c**). In keeping with prior  
114 studies, clinical labs for MIS-C patients showed high ferritin, b-type natriuretic peptide (BNP),  
115 troponin, c-reactive protein (CRP), soluble CD25, IL-6, and IL-10 (**Figure 1d** and **Table S2**).  
116 Severe patients also had high lactate, aspartate/alanine aminotransferases (AST/ALT), and  
117 creatinine, signifying the multi-organ involvement and shock state of their presentation (**Figures**  
118 **1d, S1b** and **Table S2**). One critically ill patient (P1.1) had a throat culture that was positive for  
119 group A streptococcus (**Table S3**). All of the patients improved significantly, and all but one patient  
120 have been discharged home after an average of 7 days in the hospital.



121

122 **Figure 1. Clinical features of moderate and severe MIS-C.** (a) Yale New Haven Hospital  
 123 (YNHH) timeline of total daily adult COVID-19 hospitalizations (blue) and MIS-C cumulative cases  
 124 (red). (b) Clinical time course of moderate and severe patients showing symptom onset and  
 125 treatments relative to hospital admission (Day 0). (c) PCA biplot for clinical parameters, where  
 126 available for MIS-C patients. Troponin was not measured for P13.1 was unavailable, and so this  
 127 patient was excluded from PCA. (d) Clinical laboratory data for the indicated analyte. Normal  
 128 range represented by gray shading. BNP: B-type natriuretic peptide; CRP: C-reactive protein;  
 129 ALC: absolute lymphocyte count; AST: aspartate aminotransferase; ALT: alanine  
 130 aminotransferase; WBC: white blood cells; CKD: chronic kidney disease; CHF: chronic heart  
 131 failure.

132

133

134 *Altered MIS-C immune cell subsets with no evidence of active viral or bacterial infection*

135 We surveyed the peripheral blood immune cell landscape of MIS-C by performing single-

136 cell RNA sequencing (scRNAseq) on samples from six pediatric/child healthy donors (C.HD),

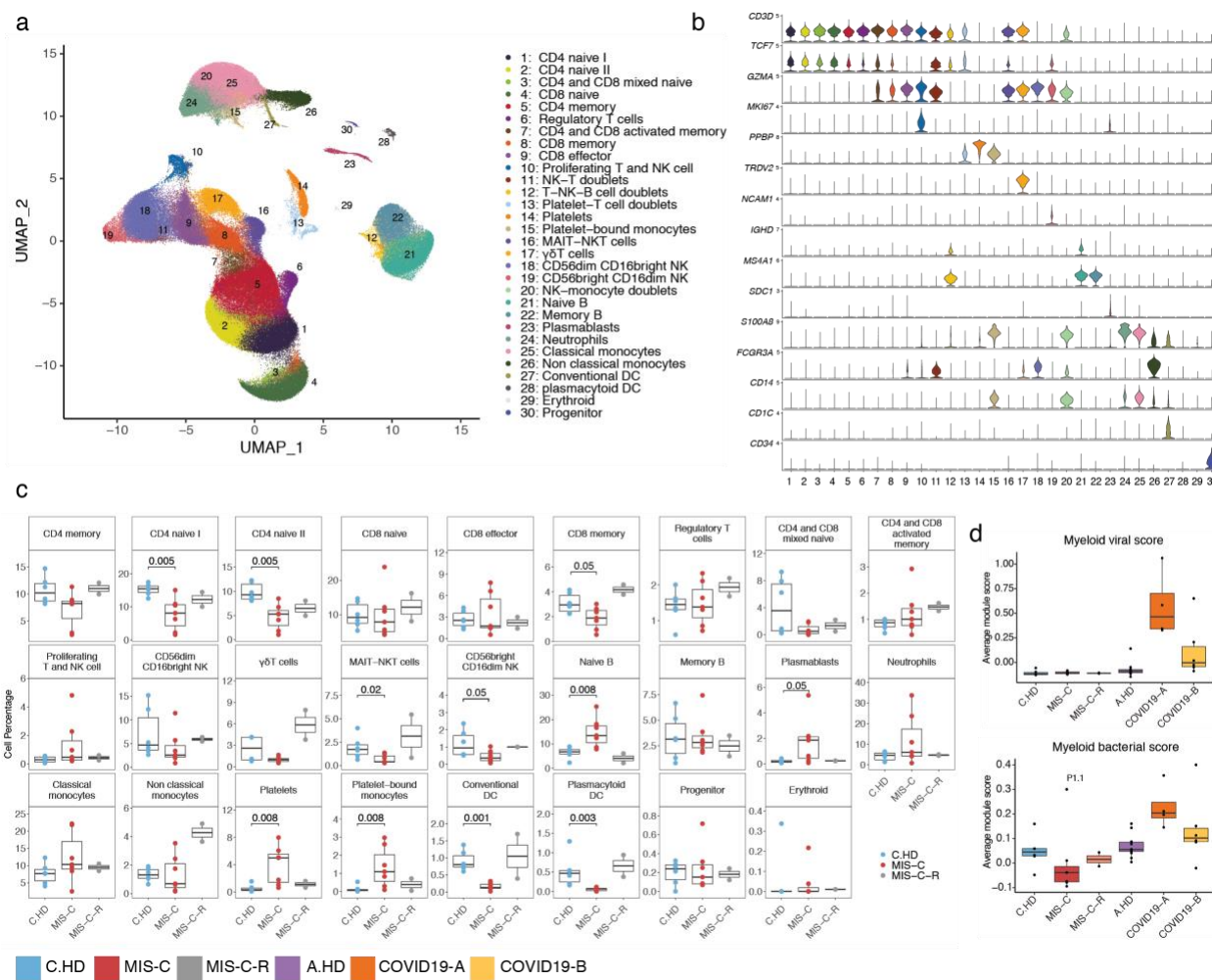
137 seven MIS-C patients, and two recovered patients (MIS-C-R). We also incorporated samples from

138 thirteen adult healthy donors (A.HD) and adult COVID-19 patients from early (COVID19-A:  
139 median of 7 days after symptom onset; n = 4) and late timepoints (COVID19-B: median of 16  
140 days after symptom onset; n = 6) from our recent study (**Figure S1d** and **Table S4**)<sup>19</sup>.

141 We performed integrative analysis to harmonize all 38 single-cell gene expression (GEX)  
142 datasets, followed by graph-based clustering and non-linear dimensionality reduction using  
143 uniform manifold approximation and projection (UMAP) to visualize communities of similar cells.  
144 We resolved 30 distinct PBMC cell types (**Figure 2a-b** and **S2a-b**). Additionally, we performed  
145 Cellular Indexing of Transcriptomes and Epitopes by Sequencing (CITE-seq) on fresh PBMCs  
146 isolated from two MIS-C patients and three A.HD, allowing 189 surface antibody phenotypes to  
147 be resolved at a single-cell level together with GEX (**Table S5**)<sup>20</sup>. To annotate memory and naïve  
148 T cell GEX-based clusters, we exploited ADT signals for CD45RO and CD45RA. We also  
149 confirmed annotations of low-density neutrophils (retained after PBMC isolation) and mature NK  
150 cells using CD66d and CD57 markers, respectively (**Figure S2c**). We subsequently determined  
151 differences in cell type percentages among the pediatric cohorts (**Figures 2c** and **S2d**). Of note,  
152 naïve CD4 T cells were decreased in the peripheral blood of MIS-C patients compared to C.HD.  
153 Naïve B cells and platelets were markedly increased, and conventional dendritic cells (cDCs) and  
154 plasmacytoid dendritic cells (pDCs) were decreased in MIS-C compared to C.HD. We additionally  
155 leveraged scRNAseq GEX data to map significant changes in ligand-receptor connectivity in MIS-  
156 C compared to C.HD (**Figure S2e**), finding that ligands and receptors involved in diapedesis and  
157 inflammation are coordinately up in MIS-C, including SELPG-ITGAM and MMP9-ITGB2.

158 To understand the possible viral or bacterial triggers for acute MIS-C onset, we evaluated  
159 well-defined signatures of respiratory viral and bacterial infections<sup>21</sup>. We detected a robust anti-  
160 viral signature in myeloid cells in COVID19-A but not in the MIS-C cohort (**Figures 2d** and **S2f**).  
161 Similarly, there was no evident bacterial signature in MIS-C compared to C.HD, with the exception  
162 of P1.1, who was confirmed to have strep throat at the time of MIS-C diagnosis (**Figure 2d** and  
163 **Table S3**). To determine whether an active herpesvirus could be found in patients with MIS-C,

164 we created viral reference transcriptomes for Epstein Barr Virus (EBV) and Cytomegalovirus  
 165 (CMV) for alignment of sequencing reads from our pediatric cohort. We did not identify counts  
 166 aligning to these transcriptomes, with the few cells that appear positive for counts likely the result  
 167 of mis-alignment (**Figure S2g**). Thus, peripheral blood cells in MIS-C patients show significant  
 168 alterations, despite no direct evidence for an active viral or bacterial infection during acute illness.



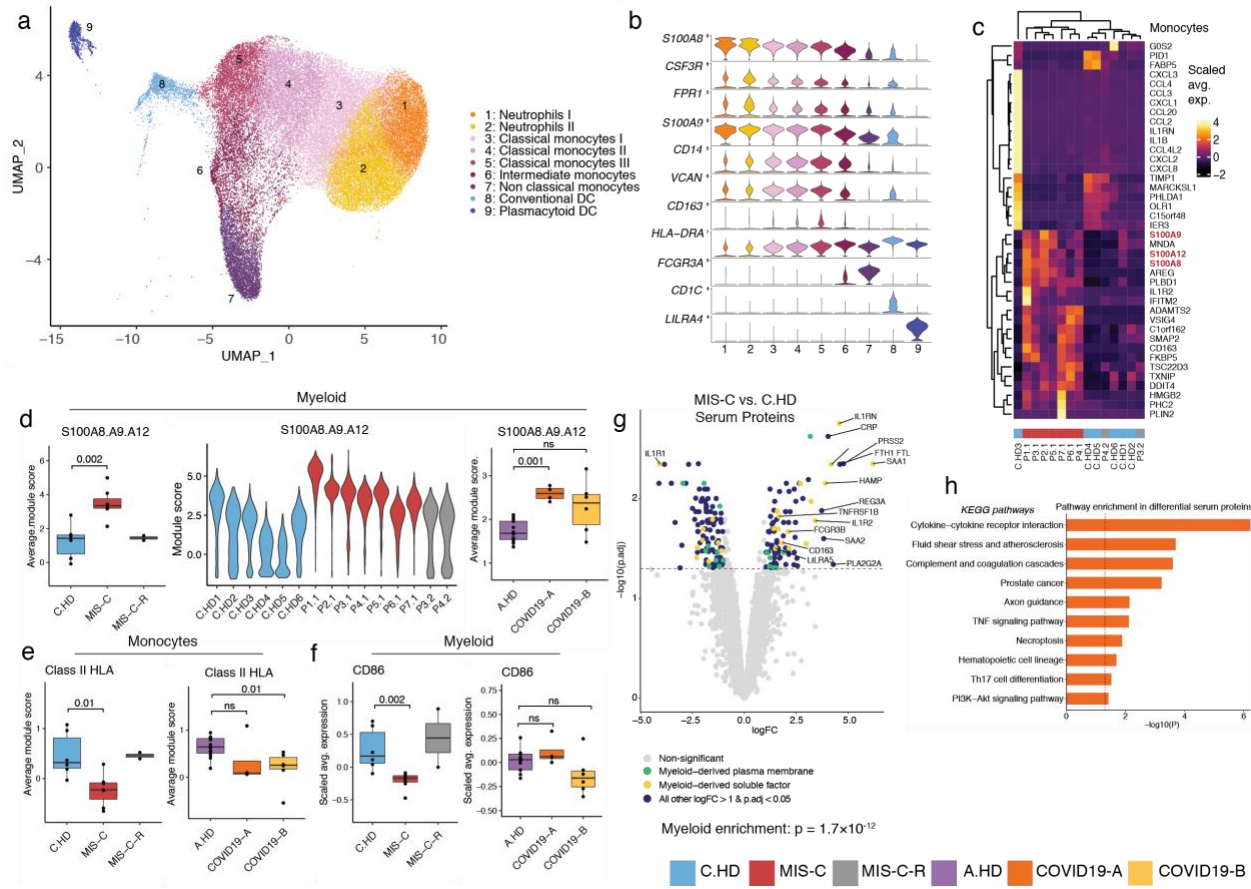
169 **Figure 2. Altered MIS-C immune cell subsets with no evidence of active viral or bacterial**  
 170 **infection.** (a) Peripheral blood mononuclear cell (PBMC) UMAP of integrated samples from  
 171 pediatric healthy donors, adult healthy donors, MIS-C patients, and COVID-19 patients. (b)  
 172 Violin plots of key PBMC cell lineage markers. Y-axis represents normalized feature counts. (c)  
 173 Distributions of peripheral blood cell frequencies across pediatric cohorts, based on cell types  
 174 inferred from scRNA-seq. A non-parametric two-sided Wilcoxon test was used to assess  
 175 statistical significance between the C.HD and MIS-C groups. (d) Donor distributions of viral and  
 176 bacterial scores in myeloid cells. Module scores are calculated for each cell and averaged per  
 177 donor.  
 178

179

180 *Elevated alarmin expression in myeloid cells with post-inflammatory phenotypic changes*

181 To investigate innate immune contributions to MIS-C, we sub-clustered monocytes,  
182 neutrophils, and dendritic cells (**Figure 3a-b**). We additionally evaluated differentially expressed  
183 genes (**Table S6**) in neutrophils and monocytes, and found a shared up-regulation of the alarmin-  
184 related S100A genes<sup>22</sup>, in particular, *S100A8*, *S100A9*, and *S100A12* (**Figures 3c-d** and **S3d**).  
185 Consistent with previous scRNAseq studies, COVID19-A samples also showed an elevated  
186 S100A score compared to A.HD (**Figure 3d**)<sup>19</sup>. Pathway enrichment on shared down-regulated  
187 genes in monocytes and neutrophils revealed a significant reduction in antigen-presentation and  
188 processing, and as in COVID-19<sup>23</sup>, MIS-C patients had significantly reduced HLA class II (HLA-  
189 DP, DQ, and DR) expression (**Figure 3e** and **S3b-d,f**). Moreover, MIS-C but not COVID-19  
190 patients exhibited down-regulation of *CD86* (**Figures 3f** and **S3e**). This was also evident by flow  
191 cytometry of pediatric PBMCs (**Figure S3g**). To comprehensively define the serum proteome  
192 landscape in MIS-C, we profiled nearly 5,000 serum proteins in three MIS-C patients (P1.1, P2.1,  
193 P3.1) and four pediatric healthy donors using SomaScan technology (**Figure 3g, S3h**). Overall,  
194 there was a significant enrichment in myeloid-derived proteins among the differentially expressed  
195 proteins in serum ( $p = 1.7 \times 10^{-12}$ ) (**Figure 3g**). Moreover, pathway analysis of differential proteins  
196 in the serum revealed enrichment of terms associated with 'Cytokine-cytokine receptor  
197 interaction', 'Fluid shear stress and atherosclerosis', and 'Complement and coagulation  
198 cascades', which are consistent with the inflammatory phenotype in the patients (**Figure 3h**). To  
199 understand the impact of up-regulated serum proteins on immune cells, we performed  
200 connectivity analysis to link upregulated serum ligands with receptors expressed in PBMCs of  
201 MIS-C patients (**Figure S3i**). This analysis highlights CXCL10-CXCR3, which is known to be  
202 involved in leukocyte trafficking to inflamed tissues, as a potentially relevant axis in MIS-C<sup>24,25</sup>.  
203 Thus, gene expression programs in myeloid cells from MIS-C patients are characterized by  
204 increased S100A alarmin expression and decreased antigen presentation that we hypothesize to

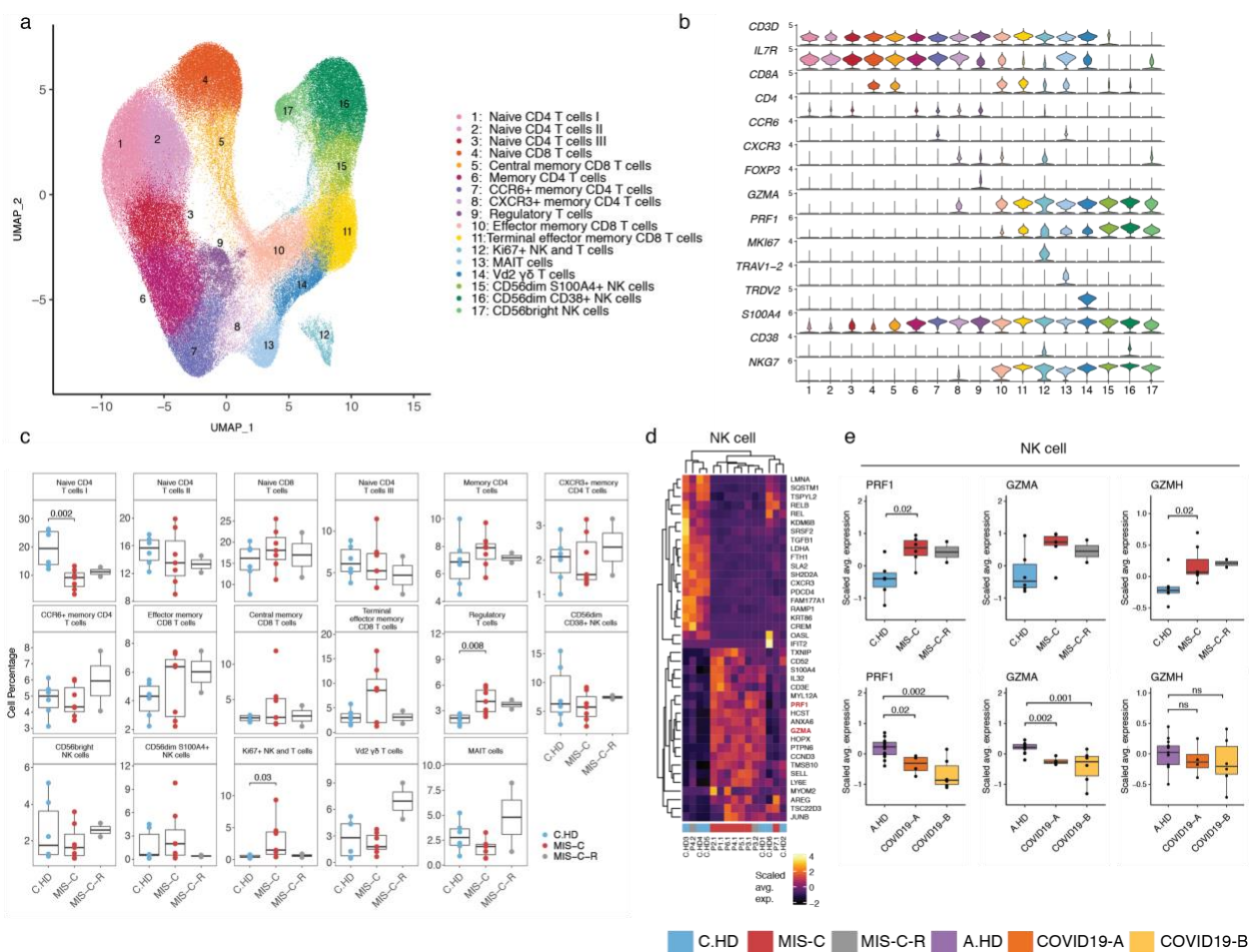
205 be a post-inflammatory feedback response. Moreover, the serum proteome in MIS-C patients is  
 206 consistent with inflammatory myeloid responses and potential endothelial cell activation.



207  
 208 **Figure 3. Innate inflammation in MIS-C with elevated myeloid alarmins in the S100A family.**  
 209 (a) Myeloid cell sub-clustering UMAP. (b) Key markers delineating myeloid clusters. (c) Heatmap  
 210 representing top 20 up- and down-regulated differentially expressed genes in monocytes between  
 211 MIS-C and C.HD. (d) A module score for *S100A8*, *S100A9*, and *S100A12* is computed across  
 212 pediatric donors and adult healthy donors in all myeloid cells depicted in UMAP. As above, module  
 213 scores are averaged per donor, and statistical significance between cohorts is computed using a  
 214 two-sided non-parametric Wilcoxon test. (e) HLA class II score including *HLA-DP*, *DQ*, and *DR*  
 215 molecules (see methods) is computed across adult and pediatric donors as above. (f) *CD86*  
 216 expression depicted across pediatric and adult donors in myeloid cells. (g) Volcano plot showing  
 217 differentially up- and down-regulated serum proteins between MIS-C (n=3) and pediatric healthy  
 218 donors (n = 4). Molecule annotations are color-coded and genes of interest are labeled in black  
 219 text. IL-1RN, an up-regulated protein in MIS-C, likely corresponds to anakinra treatment.  
 220 Significance of enrichment is calculated using Fisher's exact test. (h) Pathway analysis of  
 221 differential proteins in serum analysis between MIS-C (n=3) and C.HD (n=4).  
 222

223 *Increased cytotoxicity genes in NK cells from MIS-C patients*

224 To further define the T and NK cell states in MIS-C, we sub-clustered T and NK cells  
225 (**Figures 4a-b** and **S4a-b**). Marked differences were observed in cell type proportions of  
226 regulatory T cells and proliferating T and NK cells in MIS-C compared to C.HD (**Figure 4c**). To  
227 assess the potential for a superantigen response among T cells, we scored a defined signature  
228 of superantigen genes, which was not altered in MIS-C compared to C.HD (**Figure S4c**)<sup>26</sup>.  
229 However, differential gene expression analysis in the NK cell subset revealed a significant up-  
230 regulation of *PRF1*, *GZMA*, and *GZMH* cytotoxicity-related genes in MIS-C compared to C.HD,  
231 with high expression levels retained in recovered patients (**Figures 4d-e** and **S4d-e,g**). *CCL4*,  
232 produced by activated NK cells, was also up-regulated in MIS-C (**Figure S4f**). An analysis of T  
233 cells revealed a trend toward increases cytotoxicity gene expression in memory CD8 cells (**Figure**  
234 **S4d,h**). Additionally, *ITGB7*, an integrin subunit supporting lymphocyte infiltration of the gut  
235 through MADCAM1 binding<sup>27</sup>, was up-regulated in memory CD8 T cells (**Figure S4h**). Upon  
236 performing TCR diversity analysis, we found that a subset of MIS-C patients exhibited a decrease  
237 in memory and proliferating CD4 T cell clonal diversity, possibly indicating clonal expansion.  
238 However, no evidence of clonal expansion was seen in MIS-C CD8 cells. By contrast, COVID-19  
239 patients exhibited markedly lower TCR diversity in both CD8 and CD4 cells (**Figure S4i**). Thus,  
240 NK cells, and to a lesser extent CD8 T cells, exhibit elevated cytotoxicity features with potential  
241 relevance for tissue damage.



242

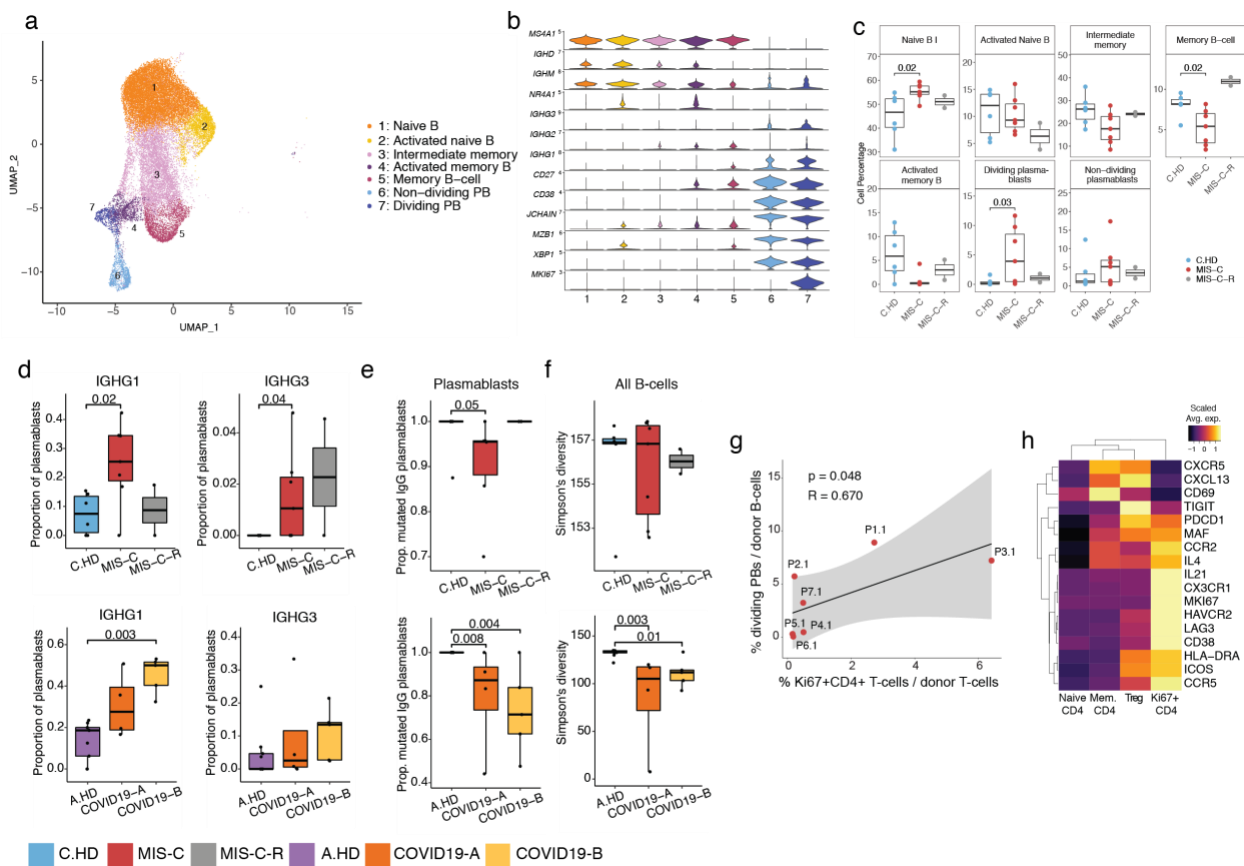
243 **Figure 4. Increased cytotoxicity signatures in NK cells from MIS-C patients.** (a) T cell sub-  
 244 sub-clustering UMAP. (b) Violin plot depicting key T and NK cell markers for cluster delineation. (c) T  
 245 and NK compositions across pediatric cohorts. (d) Heatmap representing top 20 up- and down-  
 246 regulated differentially expressed genes in NK cells between MIS-C and C.HD. Highlighted are  
 247 genes associated with cytotoxicity. (e) *PRF1*, *GZMA*, and *GZMH* expression in NK cells in MIS-  
 248 C compared to C.HD and MIS-C-R donors. Scaled average expression was calculated for each  
 249 donor. A two-sided Wilcoxon test was calculated for statistical significance between cohorts.  
 250

251 *Elevated IgG plasmablasts in MIS-C*

252 To investigate whether an ongoing humoral response could underpin acute MIS-C  
 253 immunopathology, we sub-clustered annotated B cells (Figure 5a-b). We found a notable  
 254 increase in proliferating (Ki67+) plasmablasts, which express apoptosis genes consistent with  
 255 short-lived plasmablasts, in MIS-C compared to C.HD (Figures 5c and S5a-b)<sup>28</sup>. We performed  
 256 differential expression analysis between naïve B cells of MIS-C and C.HD, and found an

257 enrichment of the KEGG B cell signaling pathway among differentially up-regulated genes (**Figure**  
258 **S5c-d**). We next assessed antibody isotype, clonotypic diversity, and somatic mutation (SHM) of  
259 B cell receptors (BCRs). In memory B cells, the proportion of IgM B cells was increased in MIS-  
260 C (**Figure S5e**). Of note, the proportion of plasmablasts expressing IgG1 or IgG3 was elevated in  
261 MIS-C (**Figures 5d, S5f**), and a smaller proportion of plasmablast IgG clones in MIS-C and  
262 COVID-19 patients harbored mutated BCR variable regions (defined as >1% nucleotides mutated  
263 relative to germline) compared to age-matched controls (**Figure 5e**)<sup>13,29</sup>. Moreover, a subset of  
264 MIS-C patients exhibits lower BCR clonal diversity – consistent with clonal expansion – when  
265 compared to C.HD, though this relationship is not as consistent as that between COVID-19  
266 patients and A.HD (**Figure 5f**).

267 To examine potential drivers of this plasmablast response, we looked at correlates in the  
268 CD4 T cell response. Indeed, we found a positive correlation between proliferating Ki67+ CD4 T  
269 cells and Ki67+ plasmablasts (**Figures 5g and S5g**). Gene expression analysis of Ki67+ CD4 T  
270 cells revealed low *CXCR5*, but high *ICOS*, *PDCD1*, *MAF*, and *IL21* as well as chemokine  
271 receptors for homing to inflamed tissue including *CCR2*, *CX3CR1*, and *CCR5* (**Figure 5h, S5h**).  
272 These cells appear to be phenotypically similar to T peripheral helper cells seen in some  
273 autoimmune conditions<sup>30</sup>. Together, these data indicate that plasmablasts in MIS-C patients are  
274 expanded, correlate with proliferating CD4 T cells with putative B cell-helper function, and more  
275 frequently harbor IgG1 and IgG3 antibody isotypes compared to C.HD.



277 **Figure 5. MIS-C patients have increased proliferating plasmablasts harboring IgG1 and**  
 278 **IgG3 and a coordinated CD4 T cell response. (a)** B cell sub-clustering UMAP. **(b)** Violin plots  
 279 for key B cell markers delineating naïve, memory, and plasmablast subsets. **(c)** Distributions of B  
 280 cell frequencies within total B cells across donors. **(d)** *IGHG1* and *IGHG3* isotype frequencies as  
 281 a proportion of plasmablasts (dividing and non-dividing) are depicted across donors. Two-sided  
 282 Wilcoxon rank sum tests were used to calculate significance. **(e)** Proportion mutated *IGHG* clones  
 283 in plasmablasts. **(f)** Simpson's diversity in all B cells computed across cohorts in pediatric cohorts  
 284 (top) and adult cohorts (bottom). Significance calculated as above. **(g)** Correlation of percentage  
 285 dividing plasmablasts/total B cells versus percentage Ki67+ CD4 cells/total T cells within the MIS-  
 286 C cohort. Ki67+ CD4 cells defined as CD4+ cells within the Ki67+ NK and T cell cluster (see  
 287 Figure 4a). Linear regression is shown with 95% confidence interval (gray area). Correlation  
 288 statistics by two-tailed Spearman rank correlation test. **(h)** Heatmap showing differential gene  
 289 expression across four subsets of CD4+ T cells, including samples from all 38 human subjects.  
 290

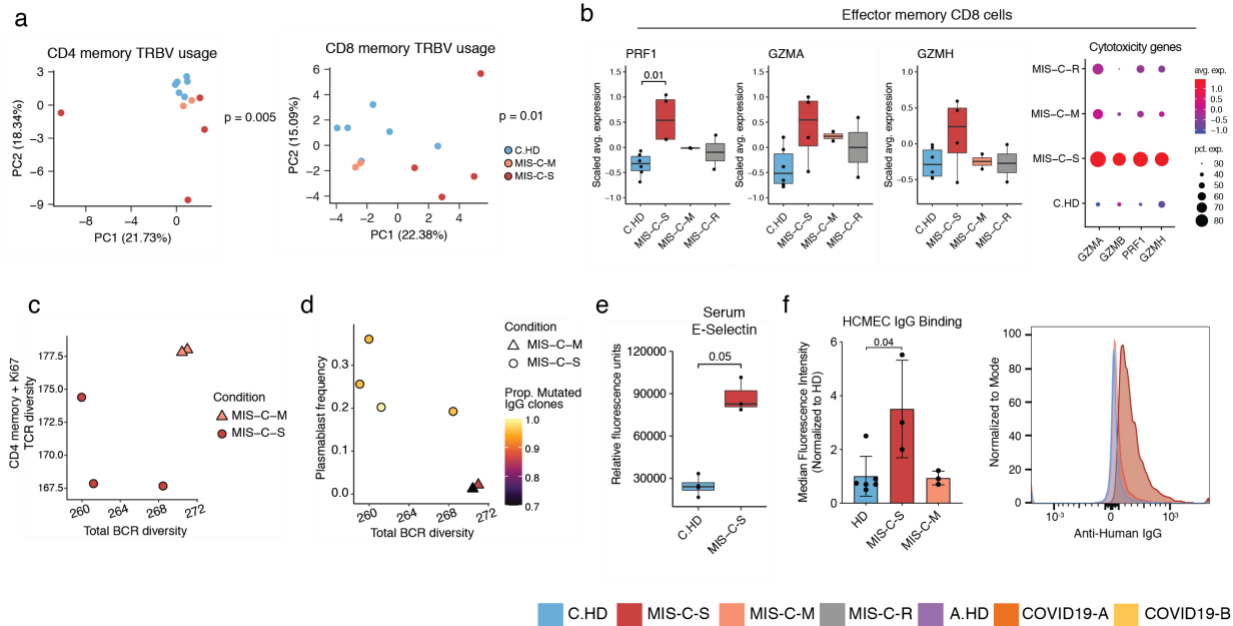
291 *Evidence for immunopathology in severe MIS-C patients*

292 Severe and moderate MIS-C patients are clinically distinct (**Table S1**). Thus, we  
 293 hypothesized immunopathology features in severe patients (here called MIS-C-S) would be more  
 294 pronounced than moderate (here called MIS-C-M) and stratified the subjects for further analysis.  
 295 To begin to assess TCR repertoire skewing from prior exposures, possibly in response to previous

296 SARS-CoV2 infection, we assessed memory T cell compartments using PCA of *TRBV* gene  
297 usage. Both CD4 and CD8 memory T cells exhibited significant skewing of the V-beta repertoire,  
298 with TRBV11 significantly enriched in MIS-C-S (n=4) compared to C.HD (n=6) or MIS-C-M (n=2)  
299 in both compartments (**Figure 6a, S6a-b**). COVID19-A and COVID19-B memory T cells did not  
300 exhibit a separation from A.HD (**Figure S6c-d**), possibly indicating a specific skewing event in the  
301 memory compartment in MIS-C. Moreover, effector CD8 T cells exhibited a significant up-  
302 regulation of *PRF1* and increases in *GZMA* and *GZMH* when comparing MIS-C-S with C.HD  
303 (**Figures 6b**). *LAG3*, an inhibitory receptor up-regulated upon T cell activation, was also increased  
304 in effector CD8 T cells (**Figure S6e**). Based on data in **Figure 5g** demonstrating a coordinated  
305 CD4 T cell and plasmablast response in some MIS-C patients, we assessed correlations further  
306 in MIS-C-S. Indeed, we found that patients with low B cell clonal diversity also had low combined  
307 Ki67+ and CD4 memory T cell diversity, suggestive of coordinated clonal expansion (**Figure 6c**).  
308 Furthermore, in MIS-C-S, we found increased plasmablast frequencies, decreased total B cell  
309 clonal diversity, and an increased proportion of mutated IgG clones, consistent with a more robust  
310 B cell response in these patients (**Figure 6d**). Consistent with these findings, the proportion of  
311 *IGHG1*- and *IGHG3*-plasmablasts was higher in MIS-C-S patients compared to controls (**Figure**  
312 **S6f**).

313         Given the distributive and cardiogenic shock in MIS-C, we aimed to investigate endothelial  
314 cell involvement. Mining the serum proteomics data from **Figure 3g** further, we noted that  
315 endothelial E-selectin, a molecule known to be expressed on inflamed endothelial cells, was also  
316 markedly up-regulated in MIS-C-S serum (**Figure 6e**)<sup>31</sup>. Next, we assessed a possible  
317 autoantibody response directed at endothelial cells. We examined binding of MIS-C serum  
318 antibodies to cultured human cardiac microvascular endothelial cells (HCMEC). Indeed, IgG from  
319 severe (P1.1, P2.1, P3.1, the latter being pre-IVIG) but not moderate (P4.1, P5.1, P11.1) MIS-C  
320 patients bound activated endothelial cells (**Figure 6f**), consistent with a potential autoimmune  
321 process. Thus, T and B cell clonal expansion, as well as cytotoxic gene expression signatures in

322 CD8 T cells, appear to correspond with severe MIS-C. Importantly, we provide functional evidence  
 323 for MIS-C autoantibody binding to activated endothelial cells relevant for severe disease  
 324 pathology.



325  
 326 **Figure 6. Distinct features of severe versus moderate MIS-C.**  
 327 (a) PCA of TRBV usage in CD4 and CD8 memory cells in the pediatric cohort. Statistical  
 328 significance calculated by permutation test (see methods) (b) *PRF1* and *GZMA* expression in  
 329 effector memory CD8+ T cells along with dot plot depicting relative average expression and  
 330 percent expression for four cytotoxicity genes (right). Wilcoxon rank sum tests were used to  
 331 calculate significance. (c) Correlation between BCR diversity and TCR diversity relating to  
 332 combined Ki67+ and memory CD4 T cells. P7.1 was excluded from TCR analysis due to low cell  
 333 numbers (see methods). (d) B-cell diversity, plasmablast frequency, and proportion of mutated  
 334 *IGHG* within MIS-C cohort. (e) Serum E-selectin in pediatric healthy and MIS-C donors. (f) Mean  
 335 fluorescence intensity (normalized to average HD) of serum IgG binding to cultured human  
 336 cardiac microvascular endothelial cells (HCMEC) by flow cytometry (left). A non-parametric  
 337 Wilcoxon rank sum test was used to calculate significance. MIS-C-S (n=3; P1-3); MIS-C-M (n=2;  
 338 P4-5); and HD (n=5; 1 C.HD and 4 A.HD). Representative histogram on the right is from P3 prior  
 339 to IVIG treatment (right).  
 340

## 341 DISCUSSION

342 We describe our findings from comprehensive analysis of MIS-C patients using single-cell  
 343 RNA sequencing, antigen receptor repertoire analysis, serum proteomics, and *in vitro* assays.  
 344 Separation of MIS-C into moderate and severe groups based on clinical criteria uncovered signals  
 345 of disease pathogenesis that otherwise would not have emerged. As previously reported<sup>11</sup>,

346 myeloid cells in MIS-C express lower HLA class II and *CD86*, molecules involved in antigen  
347 presentation, likely as a compensatory post-inflammatory feedback response. We additionally  
348 identified an up-regulation of alarmin genes including subunits of calprotectin (*S100A8* and  
349 *S100A9*) as well as EN-RAGE (*S100A12*) that function to amplify inflammatory responses.  
350 Moreover, unbiased surveying of nearly 5,000 serum proteins revealed differential abundance of  
351 many acute phase and myeloid-derived inflammatory proteins, as well as elevated endothelial E-  
352 selectin, consistent with systemic inflammation and endothelial activation.

353         What drives the cytokine storm and multi-organ damage in MIS-C? In addition to possible  
354 innate drivers described above, our analysis of lymphocytes from MIS-C patients points to three  
355 striking findings. First, NK cells and, to a lesser extent, CD8 T cells express elevated perforin,  
356 granzyme A, and granzyme H, cytotoxic molecules of relevance for tissue damage. In contrast to  
357 granzyme B, granzyme A is known to cleave pro-IL-1 $\beta$  and may directly contribute to inflammation  
358 beyond its cytotoxic function<sup>32,33</sup>. Second, B cells have an expansion of proliferating plasmablasts  
359 that fits with a potential humoral response weeks after clearance of SARS-CoV2, raising the  
360 possibility that these are autoreactive expansions of antibody-secreting cells. Third, evaluation of  
361 severe MIS-C patients identified TCR repertoire skewing among memory T cells, evidence of  
362 clonal expansion and somatic hypermutation within B cell populations, and measurable binding  
363 of serum IgG to activated cardiac endothelial cells in culture. The plasmablasts expanded in MIS-  
364 C show evidence of being short-lived with upregulated pro-apoptotic genes, which may help  
365 explain the self-resolving nature of pathology. Collectively, our data support a model in which prior  
366 SARS-CoV2 infection causes lasting immune alterations that set the stage for development of an  
367 acute and life-threatening post-infectious inflammatory episode in a fraction of children and  
368 adolescents (**Figure S7**).

369         Three main possibilities exist to explain the rare occurrence of MIS-C. First, a rare genetic  
370 predisposition could underlie disease, and future genomics investigations will be revealing on this  
371 front. Second, similarly to rheumatic heart disease, the infectious trigger could elicit adaptive

372 immune responses that, on rare occasion, cross-react with self-antigens. The rapid resolution of  
373 inflammation in MIS-C may go against this theory. Third, a rare combination of SARS-CoV2  
374 infection followed by a second microbial trigger could drive the acute MIS-C inflammatory episode.  
375 We did not find evidence of herpesvirus reactivation or peripheral blood signatures of ongoing  
376 viral or bacterial infections. Nonetheless, a tissue-specific response to an infectious trigger  
377 remains plausible, and the common feature of abdominal pain early in the course of MIS-C is  
378 suggestive of potential gut involvement and consistent with elevated *ITGB7* in T cell subsets.  
379 Further work is required to define contributions of each of these potential triggers.

380         The determinants of whether a child with MIS-C develops moderate or severe disease are  
381 also unknown and may relate to prior SARS-CoV2 viral load and immune repertoire shaping  
382 and/or differences in the putative secondary MIS-C-triggering event. Although patients with  
383 severe disease have more potential autoantibody as measured by IgG binding to cultured  
384 endothelial cells, whether this is causative of severe disease or a result of increased tissue  
385 destruction and autoantigen exposure cannot currently be determined. Moreover, by necessity,  
386 MIS-C patients are promptly treated with anti-inflammatory drugs, complicating analysis of the  
387 disease state, though we have attempted to use existing knowledge on methylprednisolone  
388 effects to inform our findings (Figure S3f)<sup>34</sup>. Although our findings in MIS-C require larger patient  
389 numbers and further testing, ideally including animal modeling, they have important implications  
390 for predicting, preventing, and treating MIS-C and offer potential paths forward for diagnostic and  
391 prognostic testing. With new waves of SARS-CoV2 outbreaks on the horizon and eventual  
392 vaccination against SARS-CoV2 in children as a critical goal, a better understanding of MIS-C  
393 drivers and immunopathology is urgently needed. Our data implicate innate and adaptive immune  
394 triggering with direct relevance for tissue destruction during acute MIS-C.

395

396 **ACKNOWLEDGMENTS**

397 The authors thank the patients and their families for participation. We are also grateful to the  
398 physicians, nurses, and hospital staff who helped care for the patients and obtain samples. The  
399 authors thank J. Pober and D. Jane-Wit for critical input, R. Montgomery for support, and G. Wang  
400 and C. Castaldi at Yale Center for Genome Analysis for 10x Genomics library preparation and  
401 sequencing services; K. Raddassi for processing scRNA-seq samples; J.L. Pappalardo for  
402 providing us the healthy adult scRNA-seq data; R. Sparks and L. Failla for assistance providing  
403 healthy pediatric samples for SomaLogic. We also thank Ms. M. Bucklin and D. Murdock for  
404 feedback and discussions. This research was supported by grants to C.L.L. from NIAID  
405 3R21AI144315-01A1S1 and Yale University. R.W.P is supported by NHLBI 1K08HL136898-  
406 01A1. AR was supported by NIAID 5T32AI007019 and NSF Graduate Research Fellowship.

407

408 **AUTHOR CONTRIBUTIONS**

409 A.R., N.N.B., and C.L.L. conceptualized the study. N.N.B., V.H., A.J.R., R.S., and J.C. consented  
410 patients and healthy donors. N.N.B, V.H., H.C. and M.L. collected blood samples and clinical  
411 information from all patients. N.N.B. and A.J.R. performed serum, plasma and PBMC isolation  
412 and cryopreservation. T.S.S., and H.A. perform scRNA-seq and CITE-seq sample preparation  
413 and cDNA generation; A.R., T.S.S., M.C., H.A., A.U., A.S., S.K., D.V.D., and C.L.L analyzed  
414 scRNA-seq gene expression data and CITE-seq data with the help of N.K. and D.A.H.; K.H. and  
415 S.K. analyzed single cell BCR data; N.L. and X.Y. analyzed single cell TCR data; W.L., B.S., N.B.,  
416 J.C. and J.T. analyzed somascan serum proteome data; M.C. performed flow cytometry analysis  
417 for patients' PBMCs; N.N.B., A.K., and R.P. performed endothelial cell experiments; A.R., N.N.B.,  
418 and C.L.L. wrote the manuscript with input from all authors; C.L.L. supervised the overall study.

419

420 **DECLARATION OF INTERESTS**

421 D.A.H. has received research funding from Bristol-Myers Squibb, Novartis, Sanofi, and  
422 Genentech. He has been a consultant for Bayer Pharmaceuticals, Bristol Myers Squibb, Compass  
423 Therapeutics, EMD Serono, Genentech, Juno therapeutics, Novartis Pharmaceuticals, Proclara  
424 Biosciences, Sage Therapeutics, and Sanofi Genzyme. Further information regarding funding is  
425 available on: <https://openpaymentsdata.cms.gov/physician/166753/general-payments>. N.K.  
426 reports personal fees from Boehringer Ingelheim, Third Rock, Pliant, Samumed, NuMedii, Indalo,  
427 Theravance, LifeMax, Three Lake Partners, RohBar in the last 36 months, and Equity in Pliant.  
428 N.K. is also a recipient of a grant from Veracyte and non-financial support from Miragen. All  
429 outside the submitted work; In addition, N.K. has patents on New Therapies in Pulmonary Fibrosis  
430 and ARDS (unlicensed) and Peripheral Blood Gene Expression as biomarkers in IPF (licensed to  
431 biotech). S.H.K. receives consulting fees from Northrop Grumman. B.S. is a former SomaLogic,  
432 Inc. (Boulder, CO, USA) employee and a company shareholder. All other authors declared that  
433 they have no competing interests.

434

435

436

437 **METHODS**

438 *Human subjects*

439 All human subjects in this study provided informed consent in accordance with Helsinki  
440 principles for enrollment in research protocols that were approved by the Institutional Review  
441 Board of Yale University. Patients were enrolled from Yale New Haven Children's Hospital (New  
442 Haven, CT) and Loma Linda Children's Hospital (Loma Linda, CA). Blood from healthy donors  
443 was obtained at Yale under approved protocols.

444

445 *COVID-19 samples*

446 COVID19-A and COVID19-B samples were provided by Unterman et al. 2020<sup>19</sup>.  
447 COVID19-A and COVID19-B blood draws were taken post-hospitalization, with a median time  
448 elapsed between timepoints of 4 days. Two samples, A.COV5, and A.COV6, only correspond to  
449 timepoint B.

450

451 *Blood sample processing*

452 Human PBMCs were isolated by Ficoll-Paque PLUS (GE Healthcare) or Lymphoprep  
453 (STEMCELL Technologies) density gradient centrifugation, washed twice in PBS, and  
454 resuspended at  $10^6$  cells/ml in complete RPMI 1640 (cRPMI) medium (Lonza) containing 10%  
455 FBS, 2 mM glutamine, and 100 U/ml each of penicillin and streptomycin (Invitrogen). PBMCs  
456 were used fresh or cryopreserved in 10% DMSO in FBS and thawed prior to use. Serum was  
457 isolated by centrifugation of serum tubes and saving the supernatant in aliquots which were flash  
458 frozen in liquid nitrogen prior to cryopreservation in -80C.

459

460 *Single-cell RNA-sequencing*

461 Cryopreserved PBMCs were thawed in a water bath at 37°C for ~2 min without agitation,  
462 and removed from the water bath when a tiny ice crystal still remains. Cells were transferred to a

463 15 mL conical tube and the cryovial was rinsed with growth medium (10% FBS in DMEM) to  
464 recover leftover cells, and the rinse medium was added dropwise to the 15 mL conical tube while  
465 gently shaking the tube. Next, growth medium was added at a speed of 3-5 ml/sec, achieving a  
466 final volume of 13 mL.

467 Fresh or thawed PBMCs were centrifuged at 400 g for 8 minutes at RT, and the  
468 supernatant was removed without disrupting the cell pellet. The pellet was resuspended in 1X  
469 PBS with 0.04% BSA, and cells were filtered with a 30  $\mu$ M cell strainer. Cellular concentration  
470 was adjusted to 1,000 cells/ $\mu$ l based on the cell count and cells were immediately loaded onto the  
471 10x Chromium Next GEM Chip G, according to the manufacturer's user guide (Chromium Next  
472 GEM SingleCell V(D)J Reagent Kits v1.1). We aimed to obtain a yield of ~10,000 cells per lane.

473 For CITE-seq staining, lyophilized Total-seq C human cocktail (BioLegend) (**Table S2**)  
474 was resuspended with 35  $\mu$ L of 2% FBS in PBS vortexed for 10 sec and incubated for 5 min at  
475 RT. To pellet the aggregated antibodies, rehydrated antibody cocktail was centrifuged at 20,000g  
476 for 10 min just before adding to the cells. PBMCs were resuspended with wash buffer at the  
477 concentration of 10-20  $\times 10^6$  cells/ml, and 0.5  $\times 10^6$  cells were used for further staining. Cells were  
478 incubated on ice for 10 mins with 5ul of Human Fc block and 5  $\mu$ L of TrueStain Monocyte Blocker  
479 (Biolegend). Next, 10-20  $\mu$ L (0.1-0.2  $\times 10^6$  cells) were aliquoted into a new tube and incubated on  
480 ice for 30 mins with 5  $\mu$ L of Total-seq C antibody cocktail prepared as above. Cells were washed  
481 twice with wash buffer and third wash was with 2% FBS in PBS, then resuspended in 1X PBS  
482 with 0.04% BSA at 1,000 cells/ $\mu$ l and loaded onto the 10x Chromium Chip G, as described above.

483 cDNA libraries for gene expression, CITE-seq, and TCR/BCR sequencing were generated  
484 according to manufacturer's instructions (Chromium Next GEM SingleCell V(D)J Reagent Kits  
485 v1.1). Each library was then sequenced on an Illumina Novaseq 6000 platform. The sequencing  
486 data was processed using CellRanger v3.1.0.

487

488 *PBMC single-cell RNA sequencing analysis*

489 Pediatric healthy donor, MIS-C, longitudinal recovered MIS-C, adult healthy donor, and  
490 adult COVID-19 PBMC CellRanger outputs were analyzed using the *Seurat* v3.2.1 package<sup>35</sup>.  
491 These data were filtered, log-normalized, integrated, and scaled prior to dimensionality reduction  
492 and cluster identification. For each dataset, we filtered out genes that were expressed in fewer  
493 than 5 cells, and we removed low quality cells which have over 10% mitochondrial gene content  
494 and contain fewer than 200 features. To remove batch- and single-donor effects, we integrated  
495 all 38 samples into one dataset using Seurat's reference-based anchor finding and integration  
496 workflow, which is recommended by Seurat for integrating large numbers of datasets. We chose  
497 an adult healthy donor sample (A.HD3) and a MIS-C patient sample (P1.1) as references for  
498 anchor finding and integration, and used 2000 anchors and the first 30 principal components  
499 (PCs) for the integration steps. To reduce dependence of clustering on cell-cycle heterogeneity,  
500 we scored cells for cell-cycle phase based on a defined set of phase-specific genes and regressed  
501 out these genes during the scaling step.

502 Principal component analysis was performed on the scaled dataset. To define the number  
503 of principal components (PCs) to use we applied the elbow plot method and we also tested  
504 different numbers of PCs to evaluate the effects on the separation of distinct cell lineages. Based  
505 on these determinations, we chose the first 30 PCs for nearest neighbor identification and a  
506 clustering resolution of 1.0 for cluster finding. Finally, we chose UMAP as a non-linear  
507 dimensionality reduction approach to visualize clusters. To define clusters, we calculated  
508 differentially expressed genes specific to each cluster using Wilcoxon rank sum test. Cluster  
509 specific markers were found that had an absolute logFC of at least 0.25, an adjusted p-value of  
510 less than 0.05, and were expressed in a minimum of 25% of cells in either cluster being compared.

511 Dead and dying cell clusters were identified as those with high mitochondrial gene content,  
512 low number of unique genes, and mitochondrial genes as the top cluster-specific differentially  
513 expressed genes. After removing cells belonging to these clusters, the data was re-processed  
514 using the same parameters above and clusters were annotated using cluster specific differential

515 expression. All scRNA-seq analysis was done using R version 4.0.2<sup>36</sup>. All scRNA-seq plots were  
516 done using *ggplot2* v3.3.2<sup>37</sup>.

517

#### 518 *CITE-seq analysis*

519 Of the 38 samples, 5 included CITE-seq data. After integrating all of the datasets in both  
520 the PBMC and sub-clustering analyses, we used a subset of our Seurat object corresponding to  
521 these 5 donors, and overlaid ADT information onto the GEX-based UMAP for cluster validation.  
522 ADT data was log-normalized prior to plotting feature counts.

523

#### 524 *Connectivity mapping*

525 The Connectome v0.2.2 package was used to generate a network analysis of ligand-  
526 receptor interactions predicted to be up- or down-regulated in MIS-C compared to C.HD<sup>38</sup>. PBMC  
527 clusters were included that were represented in both MIS-C and C.HD groups. We excluded  
528 clusters containing doublets and clusters where the sum of cells was fewer than 75 cells in either  
529 MIS-C or C.HD. To minimize differences in connectivity due to cell compositions between cohorts,  
530 we down-sampled our dataset. Specifically, for each cluster, we computed the sum of cells  
531 belonging to MIS-C patients or C.HD, and used the minimum of the two values to randomly  
532 sample cells within MIS-C or C.HD in the relevant cluster.

533 To annotate ligands and receptors, we used a list of annotated human ligand-receptor  
534 pairs sourced from the FANTOM5 database appended with immunological ligands and receptors  
535 created in a recent scRNAseq study<sup>19</sup>. Connectomes were created for each down-sampled  
536 cohort. An edge is determined as a ligand-receptor pair that is expressed in respective clusters  
537 at a level greater than 5% of cells, and edge-weights are determined as the sum of the scaled  
538 expression values of the markers<sup>38</sup>. The two connectomes were then compared to create a fold-  
539 change connectome, and this was then filtered to only differentially expressed genes between  
540 MIS-C and C.HD. An absolute logFC cutoff > 0.1 was employed for differential expression testing.

541 Finally, to visualize ligand-receptor interactions that are up-regulated in MIS-C, ligand and  
542 receptor interactions were plotted where both ligand and receptor connectome logFCs > 1.

543

#### 544 *EBV/CMV analysis*

545 To evaluate EBV or CMV infection of individuals in our cohort, we created combined  
546 human-viral genome references to align transcriptomic reads and counted the number of detected  
547 viral transcripts<sup>39,40</sup>. To be as permissive as possible, we used CellRanger to map reads to entire  
548 viral genomes, to capture counts originating from ORFs, intergenic regions, or initial infection.

549

#### 550 *Sub-clustering analysis*

551 Sub-clustering was done on myeloid cells, T and NK cells, and B cells. For T and NK sub-  
552 clustering the following clusters were selected: CD4 memory, CD4 naïve I, CD56dim CD16bright  
553 NK, CD8 naïve, CD4 naïve II, CD8 memory, gdT cells, MAIT and NKT cells, Regulatory T cells,  
554 CD4 and CD8 mixed naïve T cells, CD56bright CD16dim NK, Activated memory T cell,  
555 Proliferating T and NK cell, NK-T doublets. For myeloid sub-clustering the following clusters were  
556 selected: Classical monocytes, Neutrophils, Non-classical monocytes, Platelets, Platelet-T cell  
557 doublets, Conventional DC, Platelet-bound monocytes, Plasmacytoid DC, NK-monocyte  
558 doublets. For B cell sub-clustering the following clusters were selected: Naïve B, Memory B,  
559 Plasma cell, T-NK-B cell doublets. After selecting relevant clusters from the PBMC annotations,  
560 we performed the analysis as described above. The same references used to generate PBMC  
561 UMAP were applied in the reference-based integration for T and NK cell sub-clustering. For B cell  
562 sub-clustering integration, we added an additional reference (C.HD4) due to the unequal donor  
563 representation in the activated memory B cell cluster.

564 For B cell sub-clustering, the first 15 PCs were used for data integration and downstream  
565 steps, along with a clustering resolution of 0.3. A.COVS.2 was unable to be integrated into the B  
566 cell sub-clustering analysis due to low cell numbers (< 200 B cells) and was removed from this

567 analysis. For T and NK cell sub-clustering, 30 PCs were used for data integration, and 8 PCs for  
568 downstream steps, and a clustering resolution of 0.9 was used. For myeloid sub-clustering, 30  
569 PCs were used for data integration, and 15 PCs were used for downstream steps with a clustering  
570 resolution of 0.5.

571 Clusters were annotated as above. Doublet clusters were determined by co-expression of  
572 heterogeneous lineage markers (e.g. MS4A1 and CD3D) and nFeature and nCount distribution.  
573 Clusters of dead and dying cells were identified as above. Both of these classes of clusters were  
574 removed prior to finalizing the UMAPs.

575

#### 576 *Cell-type proportion plots*

577 To calculate cell frequencies based on single-cell data, we tabulated donor cells in each  
578 cluster, and divided these by the total donor representation in the UMAP. Because of the inherent  
579 heterogeneity in our cohorts, a non-parametric two-sided Wilcoxon rank-sum test was used to  
580 calculate statistical significance between MIS-C and C.HD.

581

#### 582 *DEG analysis and heatmaps*

583 Differentially expressed genes were computed between cohorts using the FindMarkers  
584 function in *Seurat*, using the same test and parameters as described above for clusters-specific  
585 marker delineation. We used a broader categories of cells to compute differential expression as  
586 follows: Monocytes (Classical monocytes I, Classical monocytes II, Classical monocytes III,  
587 Intermediate monocytes, Non classical monocytes), Neutrophils (Neutrophils I, Neutrophils II), NK  
588 cells (CD56dim S100A4+ NK cells, CD56dim CD38+ NK cells, CD56bright NK cells), CD8  
589 memory (Effector memory CD8 T cells, Central memory CD8 T cells, Terminal effector memory  
590 CD8 T cells), Naïve CD4 (Naïve CD4 T cells I, Naïve CD4 T cells II, Naïve CD4 T cells III), Memory  
591 CD4 T cells (Memory CD4 T cells, CCR6+ memory CD4 T cells, CXCR3+ memory CD4 T cells),

592 Naïve B cells (Naïve B, Activated naïve B), Memory B cells (Intermediate memory, Activated  
593 memory B, Memory B cell), Plasmablast (Non-dividing plasmablasts, Dividing plasmablasts).

594 To prioritize genes for analysis, we chose an absolute average log fold-change (logFC)  
595 cutoff of an absolute value  $> 0.5$ , and a p-adjusted value  $< 0.05$ . The top 20 up- or down-regulated  
596 genes, sorted by average logFC, were chosen to plot onto heatmaps. Heatmaps were visualized  
597 using the *ComplexHeatmap* v2.5.5 package. Correlation heatmaps were created using *Hmisc*  
598 v4.4-1 and *corrplot* v0.84.

599

#### 600 *Module scores*

601 Module scores were calculated using the `AddModuleScore` function using the default  
602 parameters<sup>41</sup>. The S100 score consists of S100A8, S100A9, and S100A12. The HLA class II  
603 score consists of HLA-DRB1, HLA-DRB5, HLA-DRA, HLA-DQA1, HLA-DQA2, and HLA-DQB1.  
604 The super-antigen score includes the following genes: IL2, CXCL9, UBD, IFNG, CXCL11, IL22,  
605 ANKRD22, IL17A, IL31RA, FAM26F, CXCL1, IL3, SLAMF8, LOC729936, XCL1, XCL2,  
606 SERPING1, SUCNR1, IL27, APOL4, FCGR1A, FCGR1B, SECTM1, CCL8, IL17F, BATF2, GBP4,  
607 and ETV7<sup>26</sup>. The viral score consists of SIGLEC1, RABGAP1L, IFI27, CADM1, RSAD2, MX1, and  
608 SERPING1<sup>21</sup>. The bacterial score consists of SMPD1, CD44, SERPING1, SPI1, HERC1, MCTP1,  
609 FOLR3, CFAP45, PRF1, CTBP1, HLA-DRB1, ARL1, OAS3, ZER1, CHI3L1, IFIT2, and IFITM1<sup>21</sup>.

610

#### 611 *Pathway analysis*

612 The MIS-C patients were acutely ill and treated with high-dose steroids, which are known  
613 to affect immune gene expression programs. To contend with this noise prior to conducting gene  
614 and pathway prioritization, we sought to remove genes that were clearly affected by steroid  
615 effects. As a reference, we used a publicly available bulk RNA-seq dataset of PBMC cell-types  
616 treated with methylprednisolone, the primary steroid administered to the MIS-C patients<sup>34</sup>. We  
617 removed steroid related genes relevant to each cell type from our gene lists, defined as having

618 an absolute logFC cutoff above 2 and p-value less than 0.05 in the steroid dataset and regulated  
619 in the same direction as genes in our dataset. Pathway analysis was then done on differentially  
620 expressed genes using the above criteria and filtering for steroid-related genes. These  
621 differentially expressed genes were inputted to Enrichr<sup>42,43</sup> to calculate enrichment of pathway-  
622 associated terms.

623

#### 624 *BCR analysis*

625 B cell receptor (BCR) repertoire sequence data were analyzed using the Immcantation  
626 ([www.immcantation.org](http://www.immcantation.org)) framework. Starting with CellRanger output, V(D)J genes for each  
627 sequence were aligned to the IMGT reference database v3.1.30<sup>44</sup> using *IgBlast* v1.13.0<sup>45</sup>.  
628 Nonproductive sequences were removed. Within each sample, sequences were grouped into  
629 clonal clusters, which contain B cells that relate to each other by somatic hypermutations from a  
630 common V(D)J ancestor. Sequences were first grouped by common IGHV gene annotations,  
631 IGHJ gene annotations, and junction lengths. Using the DefineClones.py function of *Change-O*  
632 v1.0.0<sup>46</sup>, sequences within these groups differing by less than a length normalized Hamming  
633 distance of 0.15 within the junction region were defined as clones using single-linkage hierarchical  
634 clustering<sup>47</sup>. This threshold was determined by manual inspection of the distance to nearest  
635 sequence neighbor distribution for each sample using *Shazam* v1.0.2<sup>19</sup>. These heavy-chain-  
636 defined clonal clusters were further split if their constituent cells contained light chains that differed  
637 by V and J genes. Within each clone, germline sequences were reconstructed with D segment  
638 and N/P regions masked (replaced with “N” nucleotides) using the CreateGermlines.py function  
639 within *Change-O* v1.0.0. All BCR analyses used R v3.6.1.

640 For analysis of B cell clonal diversity, we calculated Simpson’s diversity for each sample  
641 using the alphaDiversity function of *Alakazam* v1.0.2<sup>46</sup>. To account for differences in sequence  
642 depth, samples within each comparison were down-sampled to the same number of sequences,

643 and the mean of 100 such re-sampling repetitions was reported. Only samples with at least 100  
644 B cells were included.

645 To identify mutated B cell clones of different cell types and isotypes, B cell clones were  
646 further separated by cell type and/or isotype. For all BCR analysis, unless otherwise indicated,  
647 “plasmablasts” indicate pooled dividing- and non-dividing annotated plasmablasts defined by sub-  
648 clustering annotation and filtered on cells containing BCRs. These B cell clones were considered  
649 “mutated” if the median somatic hypermutation frequency of their constituent sequences was  $\geq$   
650 1%. This threshold is consistent with recent analyses of COVID-19 B cell repertoires<sup>19,48</sup>.

651

#### 652 *TCR analysis*

653 The raw sequencing reads were preprocessed using the Cell Ranger V(D)J pipeline by  
654 10XGenomics™, which assembled read-pairs into V(D)J contigs for each cell, identified cell  
655 barcodes from targeted cells, annotated the assembled contigs with V(D)J segment labels and  
656 located the CDR3 regions. Only V(D)J contigs with high confidence defined by cell ranger were  
657 included for downstream analysis. These V(D)J contigs were re-annotated by aligning them to  
658 the IMGT reference database v3.1.3041 using IgBlast v1.13.0 in the Change-O V1.0.0<sup>46</sup> pipeline.  
659 Cells with ambiguous alpha chain or beta chain and cells with no beta chains were removed. For  
660 cells with multiple alpha and/or beta chains, if any chain could be captured, we retained the chain  
661 with the largest nUMI that provided a unique chain. No sample to sample contamination was  
662 identified based on across-cell overlap of cell barcodes and contig sequences.

663 For analysis of T cell clonal diversity, in each sample, cells with identical alpha chain and  
664 beta chain sequences in the repertoire were grouped as one TCR clone. To quantify the clonal  
665 diversity, we calculated both Simpson and Shannon diversity for each sample using R package  
666 *Alakazam* 1.0.2<sup>46</sup> which describes the richness and evenness of the repertoire, respectively.  
667 When comparing the diversity between samples, to account for the differences in sequencing  
668 depth across different samples, down-sampling was conducted to make different samples have

669 the same number of sequences. For each diversity comparison, samples with less than 50  
670 sequences were excluded and all samples were randomly down sampled for 100 times to the  
671 smallest number of sequences of the remaining samples. The mean diversity across the 100  
672 times were reported and compared.

673 We selected memory CD4 and CD8 T cells; naïve CD4 and CD8 T cells and NK cells for  
674 downstream analysis. We separated Ki67+ cells into CD4 and CD8 categories and combined  
675 these with the memory CD4 and CD8 cells, respectively.

676 The principle component analysis (PCA) was performed on TRBV gene frequency  
677 within each individual using R package *stats* v4.0.2. Statistical significance of PCA clustering  
678 is determined by permutation test, where the statistic is the ratio of mean intra/inter cluster  
679 Euclidean distances among points. Mean values of the fraction of each TRBV gene per  
680 sample with error bars are used to demonstrate the differential gene usage. TRBV genes are  
681 sorted according on the difference between MIS-C-S and C.HD in descending order.

682

### 683 *Serum antibody binding to cultured endothelial cells*

684 De-identified and discarded high-titer panel reactive antigen (PRA) sera showing >80%  
685 reactivity to HLA Class-I and II antigens were collected from transplant patients at Yale New  
686 Haven Hospital's tissue typing laboratory. Healthy donor (HD) and moderate and severe MIS-C  
687 patient serum was isolated by centrifugation of serum collection tubes at 840g for 10 minutes.  
688 Supernatant was flash frozen in liquid nitrogen and stored in -80C prior to being thawed for  
689 experiments. To induce *in situ* levels of HLA antigens expression, 60% confluent human cardiac  
690 microvascular endothelial cells (HCMECs, Lonza) were pre-treated with human recombinant IFN-  
691  $\gamma$  (final concentration of 100 units/mL, 48 hours, Invitrogen) and TNF $\alpha$  (final concentration of 10  
692 ng/mL for 6-8 hours, Invitrogen) in EGM2 MV Microvascular Endothelial Cell Growth Medium-2  
693 (Lonza CC-4147). Cells were then washed with HBSS (Gibco) and treated with PRA, HD or MIS-

694 C serum in a 1:1 ratio with gelatin veronal buffer (GVB, Sigma) for 2 hours. Untreated cells were  
695 washed with HBSS (Gibco) followed by addition of GVB for 2 hours. To assess antibody binding,  
696 cells were suspended in trypsin, washed in 1% BSA PBS (FACS buffer) and pelleted by  
697 centrifugation at 1000 rpm. The cells were then incubated with goat anti-human IgG (H+L) cross-  
698 adsorbed secondary antibody, alexa fluor 594 (ThermoFisher, Catalog # A-11014) at 1:400  
699 dilution with FACS buffer. Unbound antibodies were removed by washing three times with 1xPBS  
700 (Gibco) followed by fixing with 3.7% Formaldehyde solution (T Baker catalogue# 2106-01) at room  
701 temperature. Cells were washed twice in FACS buffer and resuspended in 200-300 uL FACS  
702 buffer for flow cytometric analysis.

703

#### 704 *Serum protein analysis*

705 Relative serum protein levels were quantified by the SOMAscan v4 platform (Somalogic  
706 Inc., Boulder CO), which measures the binding of 5,284 modified single-stranded DNA aptamers  
707 (SOMAmers) to specific analytes in each sample (Gold et al., 2010). The assay and  
708 characteristics of the reagents have been described before (Emilsson et al., 2018). Briefly, 120µl  
709 aliquots of serum samples from three MIS-C, one Kawasaki , and one toxic shock syndrome  
710 (TSS) patients were placed across two 96-well plates with four age- and gender-matched C.HD,  
711 independent controls, and other samples not analyzed in this study. C.HD used in serum analysis  
712 were distinct from C.HD used in scRNAseq analysis. All samples were sent together on dry ice  
713 and assayed by Somalogic. Measurements were standardized using the default method  
714 performed by the manufacturer to first account for hybridization and assay bias within plates,  
715 followed by plate scaling and calibration to remove plate effects, and median normalization to a  
716 reference at the end. Based on a subset of 4,706 human protein analytes (representing 4,478  
717 distinct proteins) that passed quality control, the median intra-subject coefficient of variation (CV)  
718 of 3.30% from eight blinded technical replicates across two plates suggests low technical  
719 variability.

720 Serum connectivity networks were created by selecting the top 40 differentially up-  
721 regulated proteins in MIS-C compared to C.HD, and mapping them to receptors expressed in  
722 PBMC using the ligand-receptor reference used previously. We defined a receptor as being  
723 expressed in PBMCs if it is expressed in at least 25% of cells in any cluster.

724

#### 725 *Statistical tests*

726 The number of samples per group and experiment repeats, as well as the statistical test  
727 used is indicated in each figure legend.

728

729

730

731

732 **SUPPLEMENTAL INFORMATION**

733

Characteristic	All MIS-C (n=15)	Severe (n=8)	Moderate (n=7)
Age (years)	10.4 (2.6-18)	12 (3-18)	8.7 (2.6-17)
Sex: Male: Female	8:7	5:3	3:4
Race: Black	3 (20%)	1 (13%)	2 (29%)
Hispanic/ Latino	12 (80%)	7 (88%)	5 (71%)
White	0 (0%)	0 (0%)	0 (0%)
Body Mass Index (kg/m <sup>2</sup> )	23.3 (13.8-31.2)	23.7 (18.6-31.2)	22.9 (13.8-30.3)
Past Medical History*	6 (40%)	2 (25%)	4 (57%)
Known COVID+ contact	5 (33%)	1 (13%)	4 (57%)
SARS/CoV2 PCR+	6 (40%)	4 (50%)	2 (29%)
SARS/CoV2 IgG+	14 (100%)	7 (100%)**	7 (100%)
Other infection***	1 (7%)	1 (13%)	0 (0%)
<b>Clinical features</b>			
Fever	14 (93.3%)	7 (88%)	7 (100%)
<b>GI:</b>			
Abdominal pain	11 (73%)	5 (63%)	6 (86%)
Emesis	13 (87%)	7 (88%)	6 (86%)
Diarrhea	12 (80%)	8 (100%)	4 (57%)
<b>Cardiovascular:</b>			
Chest pain	3 (20%)	2 (25%)	1 (14%)
Cardiogenic Shock	6 (40%)	6 (75%)	0 (0%)
Distributive Shock	7 (46.6%)	7 (88%)	0 (0%)
<b>Neurologic:</b>			
Headache	6 (40%)	3 (38%)	3 (43%)
Confusion	3 (20%)	0 (0%)	3 (43%)
Rash	10 (67%)	6 (75%)	4 (57%)
Conjunctivitis	9 (60%)	6 (75%)	3 (43%)
Sore throat	4 (27%)	2 (25%)	2 (29%)
Muscle aches	4 (27%)	3 (38%)	1 (14%)
Lymphadenopathy	0 (0%)	0 (0%)	0 (0%)
<b>Diagnostics</b>			
<b>ECHO:</b>			
Depressed Left Ventricular function	6 (40%)	5 (63%)	1 (14%)
Coronary aneurism (z score>2)	2 (13%)	2 (25%)	0 (0%)
<b>Therapy</b>			
<b>Respiratory Support:</b>			
Intubation	2 (13%)	2 (25%)	0 (0%)
Non-invasive PPV	1 (7%)	1 (13%)	0 (0%)
Oxygen support			
Regular NC	1 (7%)	0 (0%)	1 (14%)
HFNC	2 (13%)	2 (25%)	0 (0%)

<b>Corticosteroids</b>	15 (100%)	8 (100%)	7 (100%)
<b>Intravenous Immunoglobulin</b>	13 (87%)	8 (100%)	5 (71%)
<b>Anakinra</b>	7 (47%)	5 (63%)	2 (29%)
<b>Tocilizumab</b>	1 (7%)	1 (13%)	0 (0%)
<b>Remdesivir</b>	1 (7%)	1 (13%)	0 (0%)
<b>Heparin</b>	7 (46%)	5 (63%)	2 (29%)
<b>Aspirin</b>	15 (100%)	8 (100%)	7 (100%)
<b>Antibiotics</b>	11 (73%)	7 (88%)	4 (57%)
<b>Convalescent plasma</b>	1 (7%)	1 (13%)	0 (0%)
<b>Vasoactive medication</b>	7 (47%)	7 (88%)	0 (0%)
<b>Outcomes</b>			
<b>Length of Stay, days</b>	6.9 (2-15) <sup>+</sup> n=14	8.5 (6-15) <sup>+</sup> n=7	5.4 (2-9)
<b>Death</b>	0	0	0

734 **Table S1. Patient characteristics.**

735 \* asthma, seizures, developmental delay, substance abuse/mental illness, 1 critical patient with  
736 chronic kidney disease (CKD) and chronic heart failure (CHF) diagnosed at the time of MIS-C  
737 work up.

738 \*\* 1 patient IgG not checked

739 \*\*\* 1 patient with group A strep found on throat culture

740 <sup>+</sup> Length of Stay for one patient excluded as still admitted

741  
742  
743  
744  
745

746  
747

Characteristic	All MIS-C (n=15)	Severe (n=8)	Moderate (n=7)
<b>Laboratory Tests:</b>			
Ferritin, ng/mL	2,035 (100-12,823)	3,278 (138-12,823)	614 (100-2,615)
BNP, pg/mL	12,568 (2,065->70,000) n=14	21,313 (2,653->70,000) n=7	3,823 (2,065-5,752)
Troponin, ng/mL	0.10 (<0.01-0.40) n=14	0.15 (0.015-0.40)	0.02 (<0.01-0.06) n=6
Creatinine, mg/dL	1.80 (0.31-11.17)	2.36 (0.40-11.17)	1.16 (0.31-4.70)
AST, U/L	291 (23-2,799)	395 (23-2,799)	173 (29-552)
ALT, U/L	169 (14-1,343)	225 (28-1,343)	107 (14-280)
Albumin, g/dL	2.6 (2.0-3.7)	2.3 (2.0-2.8)	3.0 (2.4-3.7)
Lactate, mmol/L	4.1 (0.9-14.0) n=12	5.2 (1.1-14.0)	1.9 (0.9-3.8) n=4
D-dimer, mg/L	5.1 (1.5-21.0)	7.0 (2.4-21.0)	3.1 (1.5-6.6)
CRP, mg/L	187 (6->300)	178 (6->300)	197 (93->300)
Absolute Lymphocyte Count, x1000/uL	0.7 (0.0-1.8)	0.6 (0.0-1.8)	0.8 (0.3-1.3)
Procalcitonin, ng/mL	12.0 (0.1-36.6) n=14	11.4 (0.1-31.3) n=7	12.6 (1.5-36.6)
CD25, pg/mL	15,723 (1,565-48,300) n=4	20,442 (2,598-48,300) n=3*	1,565 n=1
IL-6, pg/mL	45.9 (<2.0-147.0) n=9	58.5 (5.0-147.0) n=6	20.8 (1.8-58.6) n=3
IL-10, pg/mL	126.5 (7.4-259.0) n=5	137.9 (7.4-259.0) n=4	80.9 n=1
IFN $\gamma$ , pg/mL	6.3 (<4.2-13.0) n=5	6.8 (<4.2-13.0) n=4	<4.2 n=1

748 **Table S2. Clinical laboratory tests.** BNP- B-type natriuretic peptide; AST- aspartate  
749 aminotransferase; ALT- alanine aminotransferase; CRP- c-reactive protein.

750 \* 1 patient CD25 likely too high to measure  
751  
752  
753  
754  
755  
756  
757  
758  
759

ID	BMI (kg/m <sup>2</sup> )	Medical History	Other Infection	Symptoms	Immune modulation prior to blood sample
P1	19.4	None	Throat: Group A Strep	Fever, rash, conjunctivitis, abdominal pain, vomiting, diarrhea, myalgia, sore throat	Methylpred, IVIG, anakinra
P2	22	Smoker	None	Fever, rash, conjunctivitis, vomiting, diarrhea, shortness of breath	Methylpred, IVIG, aspirin, convalescent plasma, anakinra
P3	24.6	None	None	Fever, rash, conjunctivitis, abdominal pain, vomiting, diarrhea, chest pain	Remdesivir, anakinra
P4	21.4	None	None	Fever, rash, abdominal pain, vomiting, diarrhea	Methylpred, aspirin
P5	17.2	Seizures	None	Fever, abdominal pain, vomiting, diarrhea	Methylpred, aspirin
P6	29.8	DD, CKD, CHF	None	Chills, shortness of breath, cough, abdominal pain, vomiting, diarrhea, anorexia, myalgia, sore throat, headache	Methylpred, anakinra
P7	32.3	None	None	Fever, rash, fatigue, vomiting, diarrhea, headache and altered mental status	Methylpred, IVIG, aspirin, anakinra

760  
761  
762  
763  
764  
765  
766  
767

**Table S3. Characteristics of patients included in single-cell RNA sequencing.** M- male; F- female; DD-developmental delay; CKD- chronic kidney disease; CHF-chronic heart failure; Hisp-Hispanic; Methylpred- methylprednisolone; IVIG- intravenous immunoglobulin.

Sample ID	Condition	Subject ID	Time point	# days between hosp. and draw	Sex	Processing Lab	Storage	Blood shipped o/n (y/n)	# hours between draw and ficoll	Age group	Donor/Patient	ICU status	Severity
P1.1	MIS-C	P1	A	4	M	Lucas1	fresh	N	less than 3	Ped	Pt	Y	MIS-C-S
TSS	TSS	TSS	A	1	F	Lucas1	fresh	N	less than 3	Ped	Pt	Y	NA
P2.1	MIS-C	P2	A	4	M	Lucas1	fresh	N	less than 3	Ped	Pt	Y	MIS-C-S
A.HD1	A.HD	A.HD1	NA	NA	M	Lucas1	fresh	N	less than 3	Adult	HD	NA	NA
A.HD2	A.HD	A.HD2	NA	NA	F	Lucas1	fresh	N	less than 3	Adult	HD	NA	NA
A.HD3	A.HD	A.HD3	NA	NA	M	Lucas1	fresh	N	less than 3	Adult	HD	NA	NA
A.COVI.1	COVID19-A	A.COVI	A	2	M	Kaminski	cryopreserved	N	NA	Adult	Pt	N	NA
A.COVI.2	COVID19-B	A.COVI	B	6	M	Kaminski	cryopreserved	N	NA	Adult	Pt	N	NA
A.COVI.1	COVID19-A	A.COVI	A	3	F	Kaminski	cryopreserved	N	NA	Adult	Pt	N	NA
A.COVI.2	COVID19-B	A.COVI	B	6	F	Kaminski	cryopreserved	N	NA	Adult	Pt	N	NA
A.COVI.3	COVID19-A	A.COVI	A	3	M	Kaminski	cryopreserved	N	NA	Adult	Pt	N	NA
A.COVI.3	COVID19-B	A.COVI	B	15	M	Kaminski	cryopreserved	N	NA	Adult	Pt	N	NA
A.COVI.4	COVID19-A	A.COVI	A	2	F	Kaminski	cryopreserved	N	NA	Adult	Pt	N	NA
A.COVI.4	COVID19-B	A.COVI	B	6	F	Kaminski	cryopreserved	N	NA	Adult	Pt	N	NA
A.COVI.5	COVID19-B	A.COVI	B	12	M	Kaminski	cryopreserved	N	NA	Adult	Pt	Y	NA
A.COVI.6	COVID19-B	A.COVI	B	8	M	Kaminski	cryopreserved	N	NA	Adult	Pt	Y	NA
A.HD4	A.HD	A.HD4	NA	NA	M	Kaminski	cryopreserved	N	NA	Adult	HD	NA	NA
A.HD5	A.HD	A.HD5	NA	NA	M	Kaminski	cryopreserved	N	NA	Adult	HD	NA	NA
A.HD6	A.HD	A.HD6	NA	NA	M	Kaminski	cryopreserved	N	NA	Adult	HD	NA	NA
A.HD7	A.HD	A.HD7	NA	NA	M	Kaminski	cryopreserved	N	NA	Adult	HD	NA	NA
A.HD8	A.HD	A.HD8	NA	NA	F	Hafler	fresh	N	NA	Adult	HD	NA	NA
A.HD9	A.HD	A.HD9	NA	NA	F	Hafler	fresh	N	NA	Adult	HD	NA	NA
A.HD10	A.HD	A.HD10	NA	NA	F	Hafler	fresh	N	NA	Adult	HD	NA	NA
A.HD11	A.HD	A.HD11	NA	NA	M	Hafler	fresh	N	NA	Adult	HD	NA	NA
A.HD12	A.HD	A.HD12	NA	NA	F	Hafler	fresh	N	NA	Adult	HD	NA	NA
A.HD13	A.HD	A.HD13	NA	NA	M	Hafler	fresh	N	NA	Adult	HD	NA	NA
P3.1	MIS-C	P3	A	2	M	Lucas2	cryopreserved	N	less than 6	Ped	Pt	Y	MIS-C-S
P4.1	MIS-C	P4	A	2	F	Lucas2	cryopreserved	N	less than 6	Ped	Pt	N	MIS-C-M
P5.1	MIS-C	P5	A	2	F	Lucas2	cryopreserved	N	less than 6	Ped	Pt	N	MIS-C-M
P6.1	MIS-C	P6	A	3	M	Lucas2	cryopreserved	N	less than 6	Ped	Pt	Y	NA
P7.1	MIS-C	P7	A	1	M	Lucas2	cryopreserved	Y	about 24	Ped	Pt	Y	MIS-C-S
P3.2	MIS-C-R	P3	B	73	M	Lucas2	cryopreserved	N	less than 6	Ped	Pt	NA	NA
P4.2	MIS-C-R	P4	B	45	F	Lucas2	cryopreserved	N	less than 6	Ped	Pt	NA	NA
C.HD1	C.HD	C.HD1	NA	NA	F	Lucas2	cryopreserved	N	less than 6	Ped	HD	NA	NA
C.HD2	C.HD	C.HD2	NA	NA	M	Lucas2	cryopreserved	Y	about 24	Ped	HD	NA	NA
C.HD3	C.HD	C.HD3	NA	NA	F	Lucas2	cryopreserved	N	less than 6	Ped	HD	NA	NA
C.HD4	C.HD	C.HD4	NA	NA	M	Lucas2	cryopreserved	Y	about 24	Ped	HD	NA	NA
C.HD5	C.HD	C.HD5	NA	NA	M	Lucas2	cryopreserved	Y	about 24	Ped	HD	NA	NA
C.HD6	C.HD	C.HD6	NA	NA	M	Lucas2	cryopreserved	Y	about 24	Ped	HD	NA	NA

768

769 **Table S4. Meta-data for sequencing samples.**

770 Indicated are unique sample IDs, subject IDs, patient characteristics (age, sex, condition, icu status etc.), and processing conditions.

771 Also indicated are the lab from which the samples originated (where Lucas1 and Lucas2 batches were processed on different days),

772 the number of days between hospitalization and blood draw (no\_days\_bt\_hosp\_blood\_draw), and the number of hours between blood  
773 draw and processing by Ficoll (no\_hrs\_bt\_draw\_and\_ficoll).

774

775

776 **Table S5. CITE-seq panel.**

777 189 markers used for CITE-seq. Listed are the surface markers, corresponding gene names, and associated sequences.

778

779

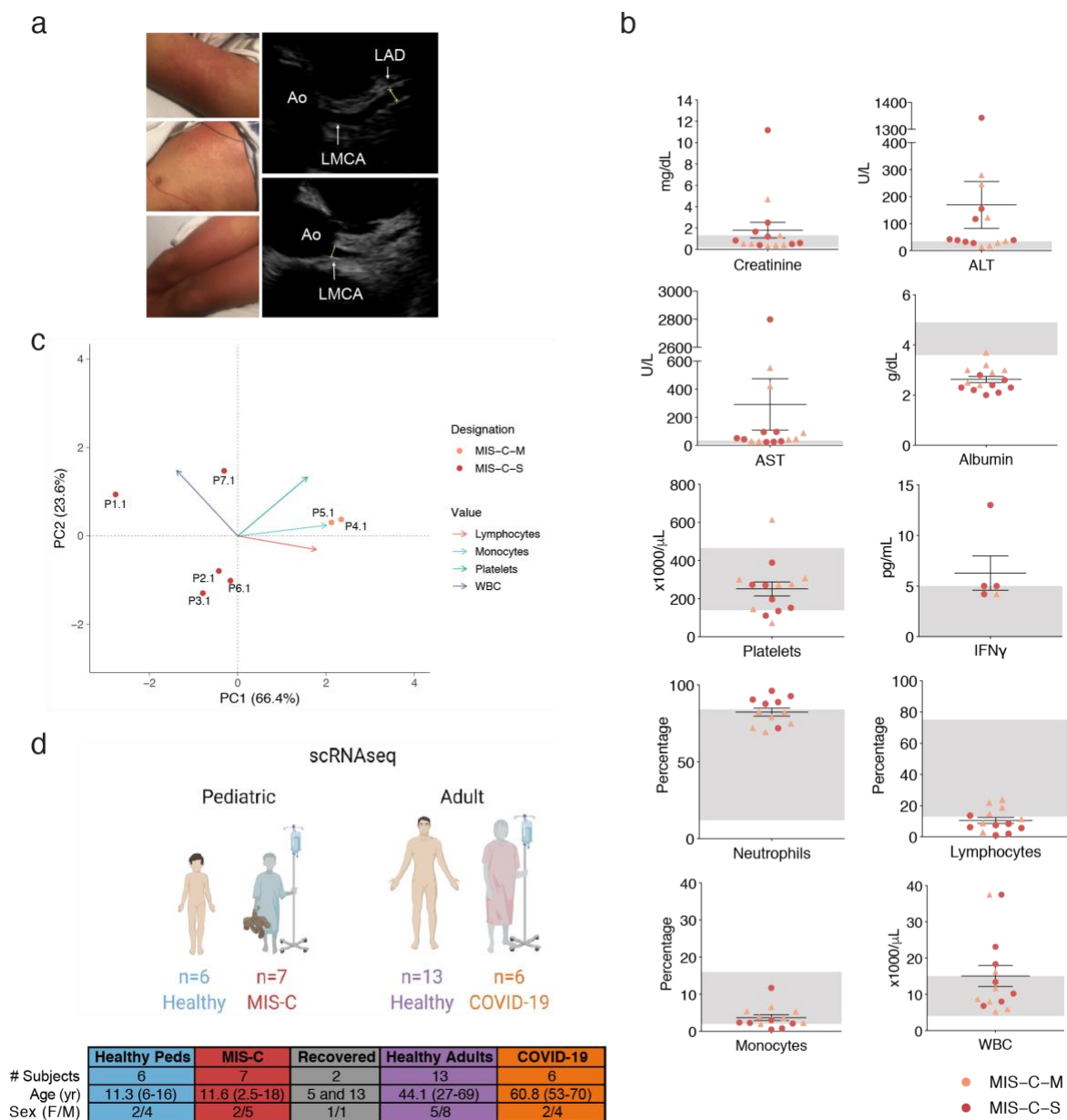
780 **Table S6. Differentially expressed genes.**

781 Differential expression markers between MIS-C and C.HD, in clusters corresponding to broad immune cell subsets. (see methods).

782 Markers gated on  $\text{abs}(\log\text{FC}) > 0.05$  and  $\text{p.adj} < 0.05$ .

783

784



785

786

787 **Figure S1. Supplemental clinical features.** (a) MIS-C rash on patient P1 and coronary aneurysm

788 in left anterior descending coronary artery, Z score of 3.51, in patient P3. Ao-aorta; LMCA- left

789 main coronary artery; LAD- left anterior descending coronary artery. (b) Acute phase laboratory

790 values (creatinine, ALT/AST, albumin, IFN $\gamma$ ) and laboratory values on the day of blood

791 sampling/protocol consent (WBC, neutrophils, lymphocytes, monocytes). Severe MIS-C (MIS-C-

792 S) is highlighted in red dots and moderate MIS-C (MIS-C-M) in light red triangles. Normal range

793 represented by gray shading. AST- aspartate aminotransferase; ALT- alanine aminotransferase;

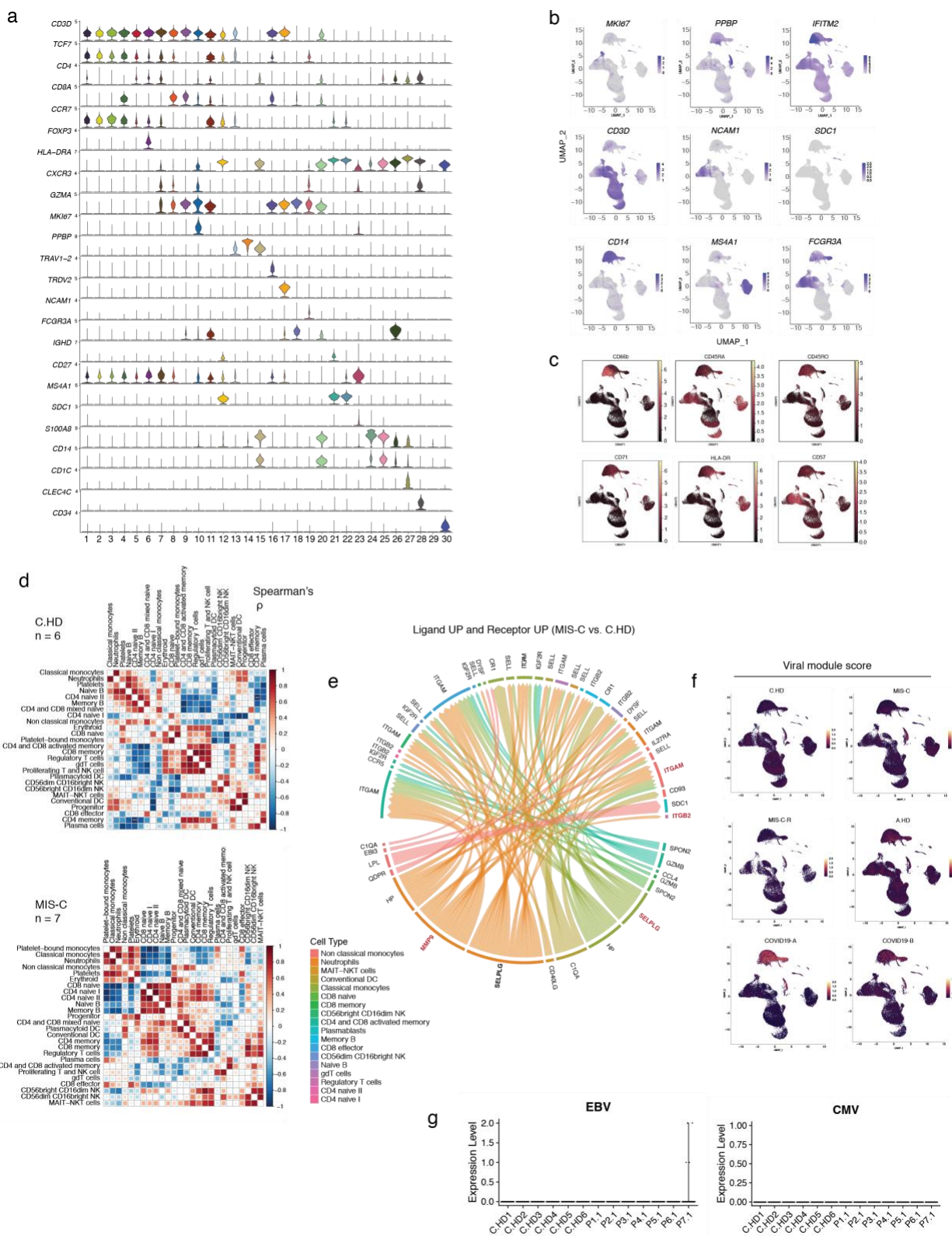
794 WBC- white blood cells. (c) PCA plot of single-cell RNA sequencing cohort separates severe and

795 moderate patients by complete blood count values at time of blood sampling. (d) Overview of

796 single-cell RNA sequencing cohorts.

797

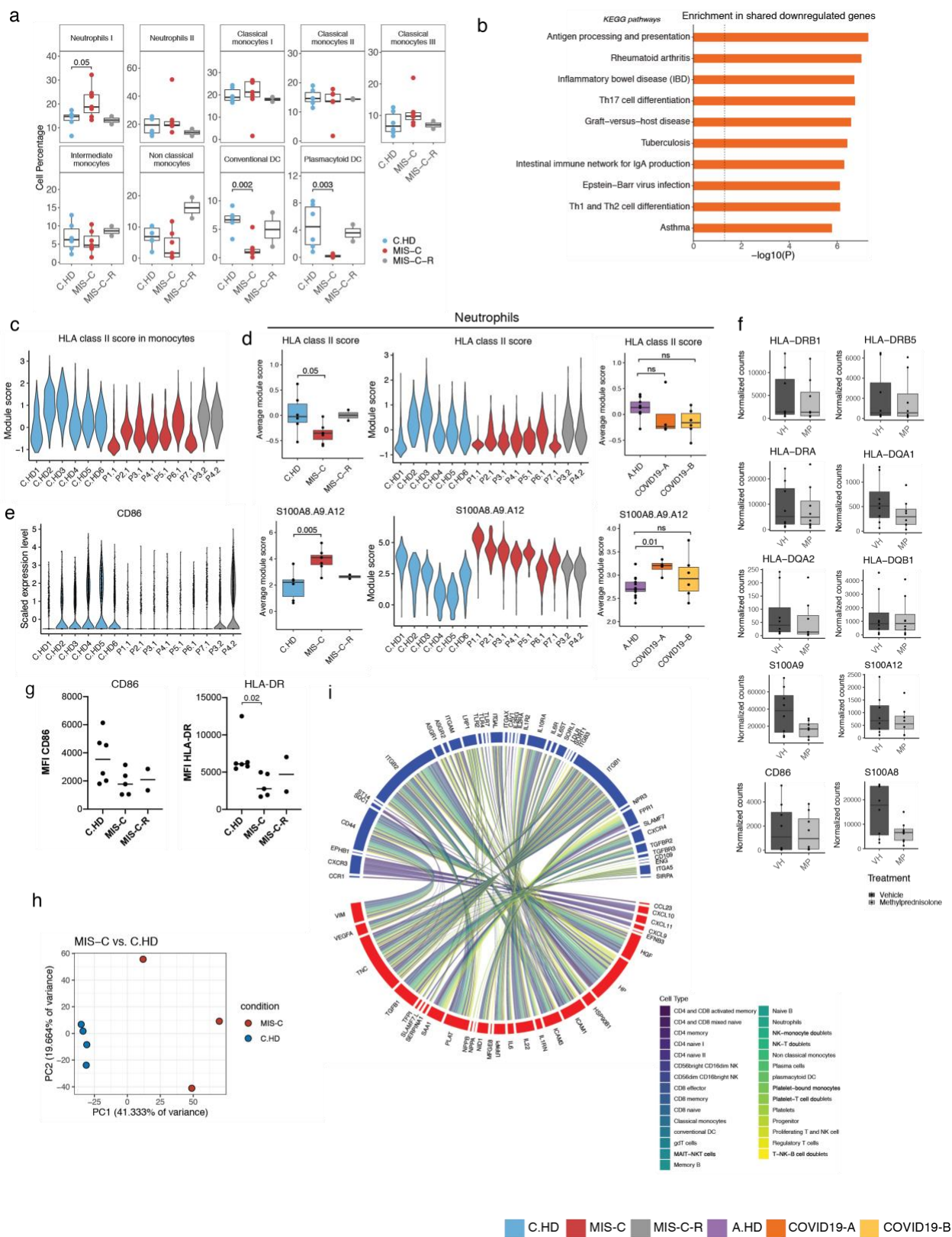
798



799  
800  
801  
802

**Figure S2. Comprehensive analysis of PBMC clusters, receptor-ligand pairs, and viral gene modules.** (a) Violin plots depicting extensive PBMC cell lineage markers, as in Figure 2b. (b) UMAP overlay of markers delineating major cell types including T cells, NK cells, plasma cells, B

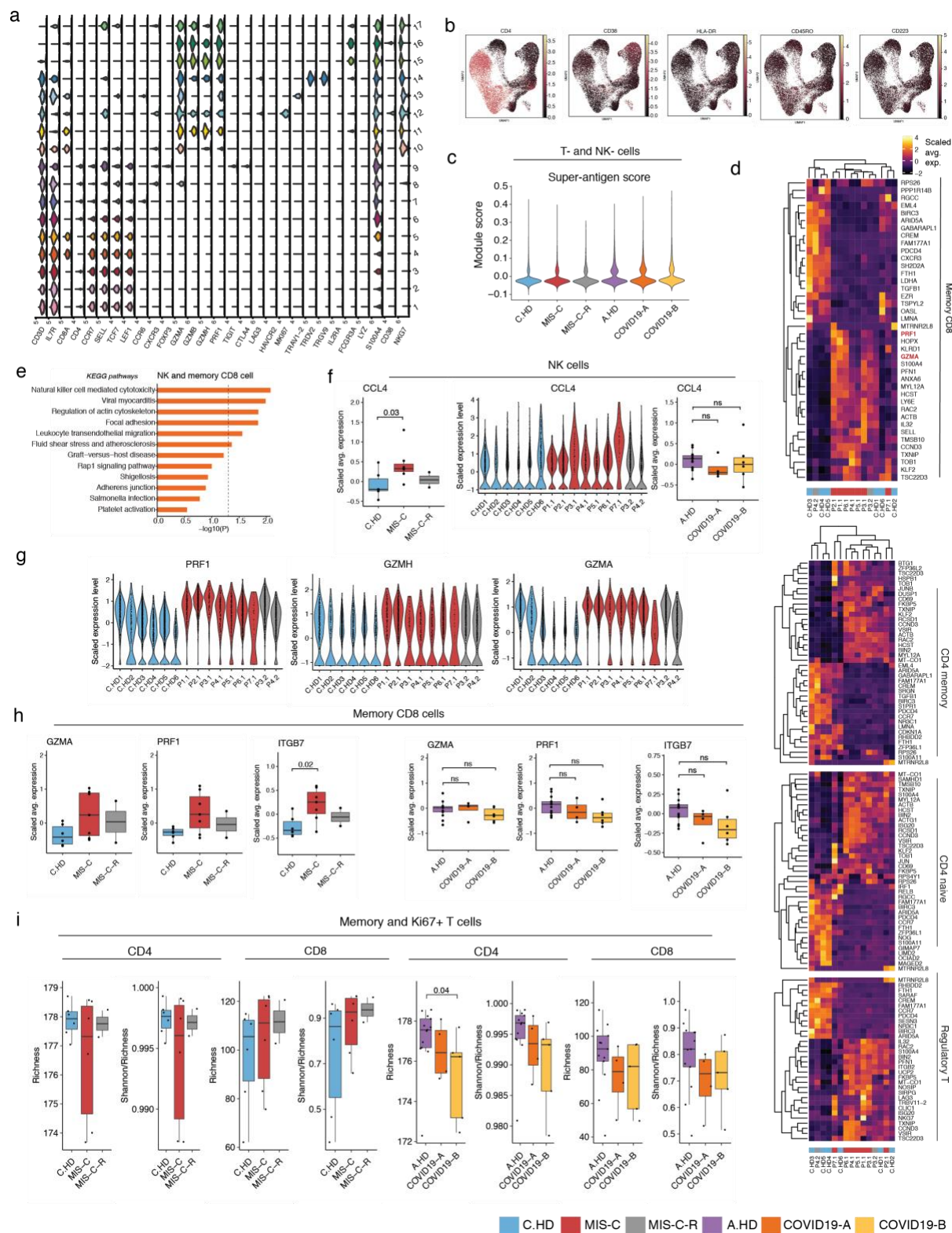
803 cells, monocytes, and neutrophils. Scale represents normalized GEX feature counts. **(c)** PBMC  
804 UMAPs with overlay of CITE-seq data. Scale represents normalized CITE-seq feature counts. **(d)**  
805 Correlation matrix of cell frequencies within C.HD (top) and within MIS-C cohorts (bottom). Scale  
806 represents Spearman's rho. P-values, where depicted, were calculated using Wilcoxon rank sum  
807 test, and adjusted for multiple comparisons using the Benjamini Hochberg procedure<sup>49</sup>. \*\*\*  
808 indicates  $p < 0.001$ . **(e)** Predicted ligand-receptor interactions from genes that are significantly  
809 up-regulated in MIS-C vs. C.HD. Highlighted are ligands and receptors involved in diapedesis  
810 and/or inflammation. **(f)** Viral and bacterial gene expression scores in PBMC UMAP, split by  
811 condition. **(g)** Counts mapping to EBV and CMV reference transcriptomes.  
812  
813



814  
815  
816  
817

**Figure S3. Supplemental myeloid cell findings and serum ligand-PBMC receptor connectome.** (a) Myeloid cell type percentages across donors. (b) Pathways enriched in down-

818 regulated differentially expressed genes shared by monocytes and neutrophils between MIS-C  
819 vs. C.HD. **(c)** HLA class II score across donors in monocytes **(d)** HLA class II score (top) and  
820 *S100A8*, *A9*, and *A12* (bottom) in neutrophils across pediatric and adult donors. **(e)** *CD86* across  
821 donors in myeloid cells. **(f)** *S100-*, *CD86*, and *HLA* gene expression changes are quantified based  
822 on a publicly available RNA-sequencing data of *in vitro* steroid treatment of myeloid cells for 6  
823 hours with methylprednisolone or DMSO<sup>34</sup>. **(g)** *CD86* and *HLA-DR* flow cytometry data of pediatric  
824 donor samples, gated on monocytes. Statistical significance computed with a two-tailed t-test. **(h)**  
825 PCA of individuals based on serum proteomic data. Conditions healthy pediatric donors (n = 4)  
826 and MIS-C patients (n = 3). **(i)** Connectivity network representing top 40 differentially expressed  
827 serum ligands and receptor pairs, where receptors are expressed in at least one PBMC cluster  
828 (minimum percentage cutoff = 0.25). Ribbon colors represent receptor-associated cell type.  
829



830  
831  
832  
833  
834

**Figure S4. Supplemental NK and T cell findings.** (a) Violin plots depicting extensive T cell sub-clustering lineage markers. (b) T cell UMAPs with overlay of CITE-seq data. (c) Super-antigen module score depicted across T and NK cells. (d) Heatmap representing top differential

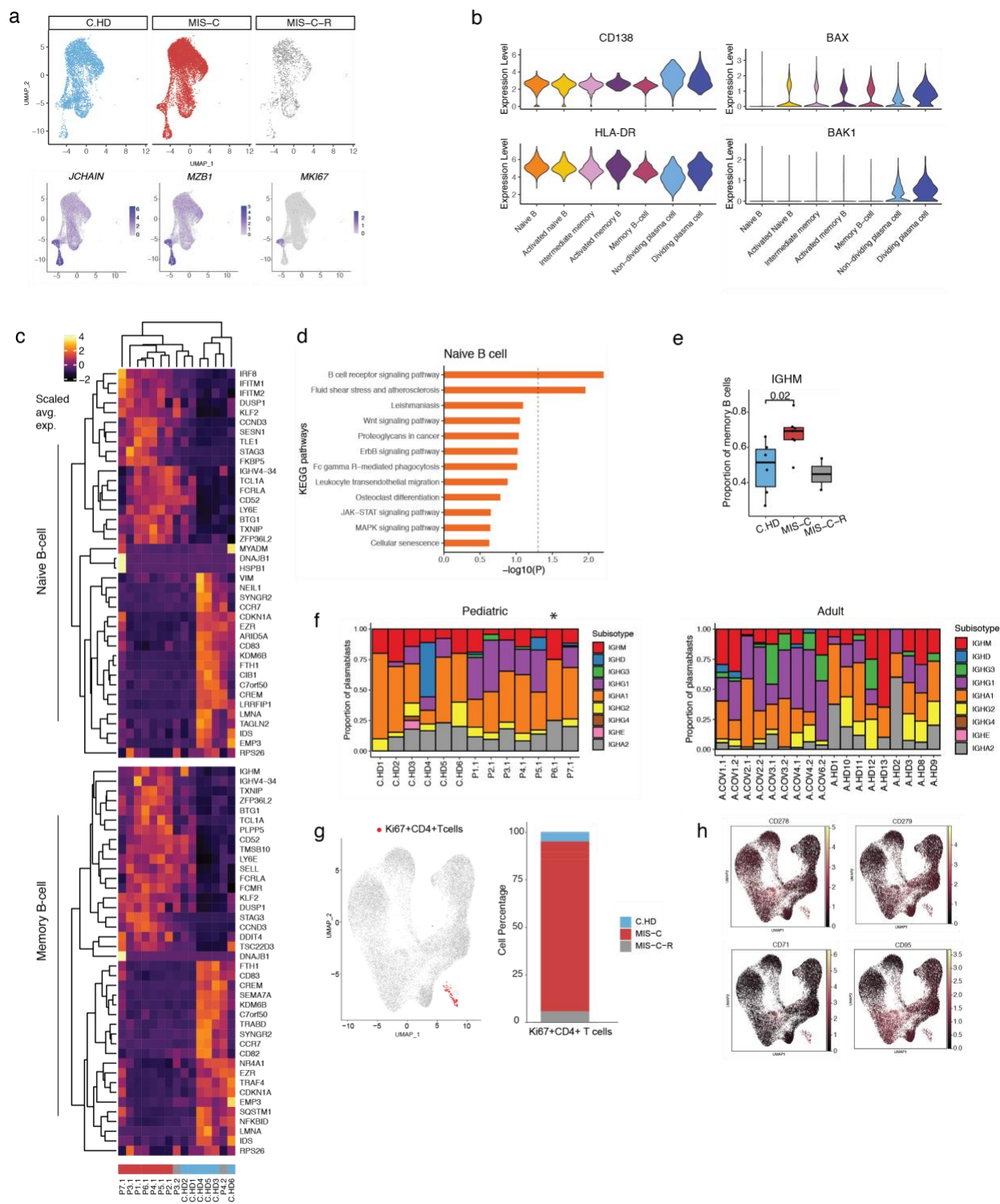
835 expressed genes between MIS-C vs C.HD in memory CD8 T cells (top) and CD4 T cell subsets  
836 (bottom). **(e)** Analysis of pathways using Enrichr for shared up-regulated genes in NK and memory  
837 CD8 T cells. **(f)** *CCL4* expression in NK cells across pediatric and adult donors. **(g)** *PRF1*, *GZMA*,  
838 and *GZMH* expression in NK cells across pediatric donors. **(h)** *GZMA*, *PRF1*, and *ITGB7* in  
839 memory CD8 cells across pediatric and adult donors. **(i)** Rarefied diversity indices (richness and  
840 evenness) of combined Ki67+ and memory T cells in TCR data analysis.

841

842

843

844

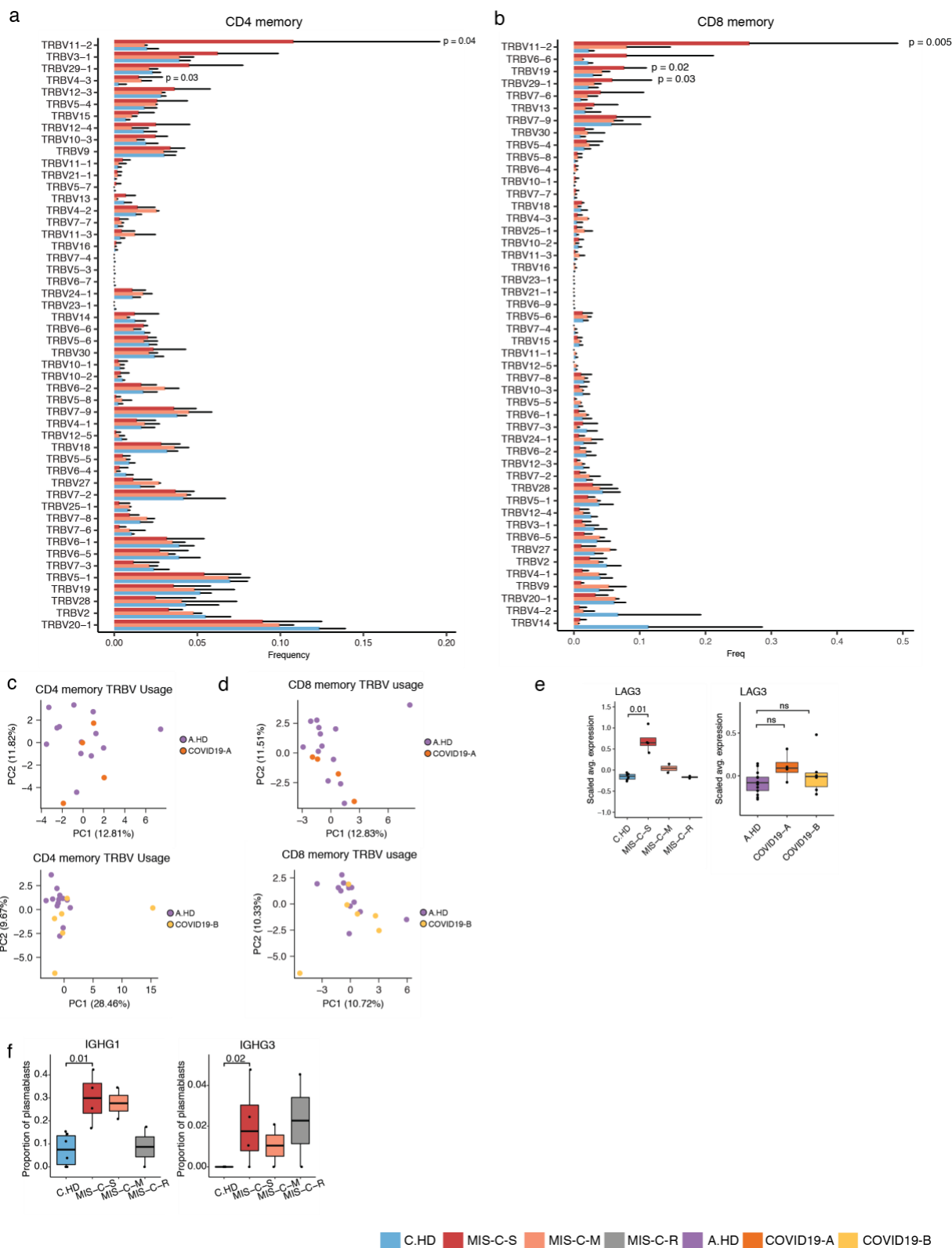


845  
846

C.HD MIS-C MIS-C-R A.HD COVID19-A COVID19-B

847 **Figure S5. Supplemental B cell findings.** (a) B cell UMAP split across pediatric conditions  
848 (C.HD, MIS-C, and MIS-C-R) (top). Marker genes delineating dividing plasmablasts are overlaid  
849 onto fully integrated UMAP (bottom). (b) Markers used to annotate short-lived plasmablasts  
850 among B cell clusters. (c) Heatmap depicting differentially expressed genes in naïve B cells and  
851 memory B cells. (d) Pathway analysis of up-regulated differentially expressed genes in naïve B  
852 cells. (e) Proportion of IGHM+ memory B cells by analysis of constant regions (f) Isotype  
853 compositions of pediatric and adult cohorts. \*P6.1 also had chronic kidney and heart disease. (g)  
854 Ki67+ CD4 T cells are labeled on T cell UMAP (left). Proportion of Ki67+ CD4 T cells across  
855 pediatric cohorts (right). (h) CITE-seq overlay on T cell UMAP depicting expression of B helper  
856 surface markers in the Ki67+ CD4 T cells.  
857

858

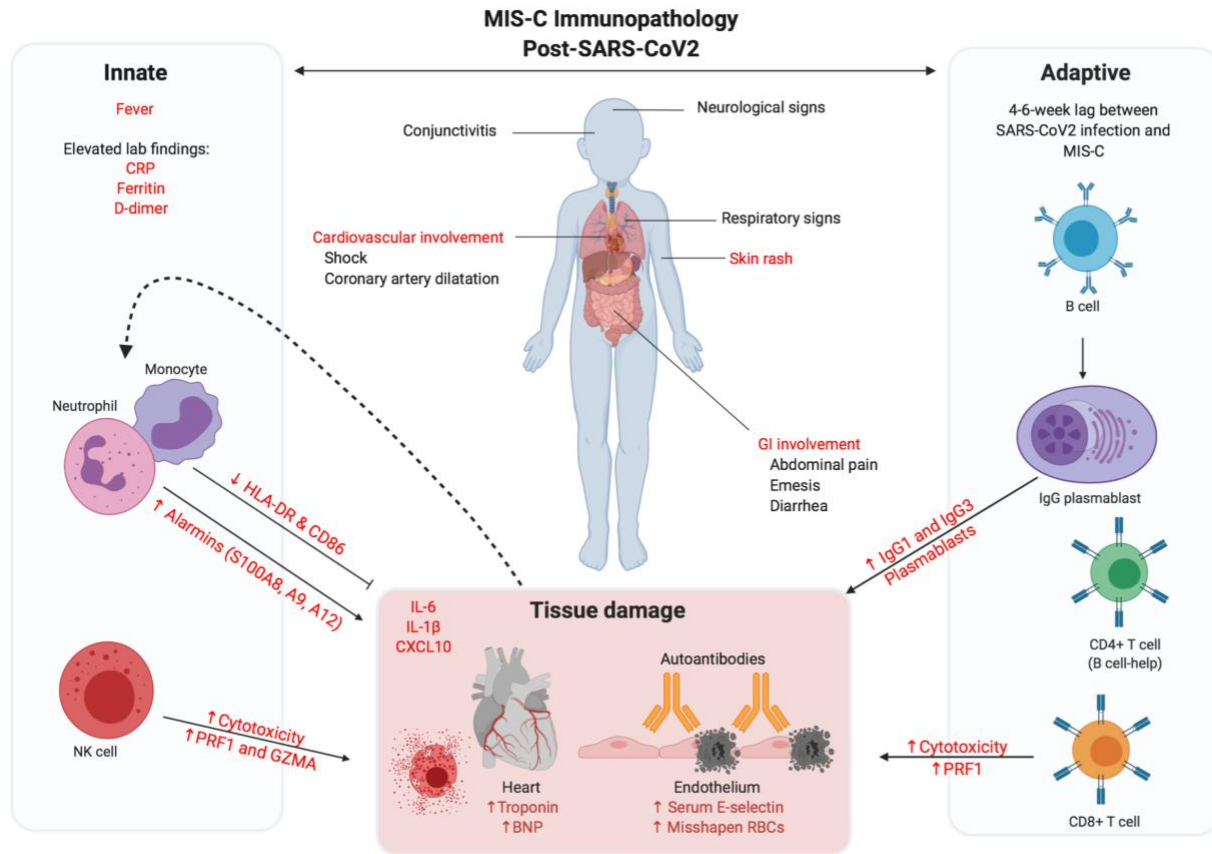


859

860

861 **Figure S6. Supplemental findings in severe MIS-C patients. (a)** Distribution of *TRBV* gene  
 862 usage in CD4 memory (see **Figure 6a**) with statistical significance computed between MIS-C-S

863 and C.HD using a two-sided Wilcoxon rank sum test. **(b)** As in (a), for CD8 memory. **(c)** PCA of  
864 *TRBV* usage in CD4 memory cells for A.HD and COVID19-A (top) and A.HD and COVID19-B  
865 (bottom). **(d)** As in (c), for CD8 memory. **(e)** *LAG3* expression across pediatric and adult donors.  
866 **(e)** Proportion of *IGHG1* and *IGHG3* plasmablasts compared between C.HD and MIS-C-S.  
867  
868



869  
870  
871  
872  
873  
874  
875  
876  
877  
878

**Figure S7. Schematic model of immunopathology drivers in MIS-C.** Figure generated with Biorender.com.

879 REFERENCES

- 880 1. Feldstein, L.R., *et al.* Multisystem Inflammatory Syndrome in U.S. Children and  
881 Adolescents. *N Engl J Med* (2020).
- 882 2. Whittaker, E., *et al.* Clinical Characteristics of 58 Children With a Pediatric  
883 Inflammatory Multisystem Syndrome Temporally Associated With SARS-CoV-2.  
884 *JAMA* **324**, 259-269 (2020).
- 885 3. Jones, V.G., *et al.* COVID-19 and Kawasaki Disease: Novel Virus and Novel  
886 Case. *Hosp Pediatr* **10**, 537-540 (2020).
- 887 4. Riphagen, S., Gomez, X., Gonzalez-Martinez, C., Wilkinson, N. & Theocharis, P.  
888 Hyperinflammatory shock in children during COVID-19 pandemic. *The Lancet*  
889 (2020).
- 890 5. Rauf, A., Vijayan, A., John, S.T., Krishnan, R. & Latheef, A. Multisystem  
891 Inflammatory Syndrome with Features of Atypical Kawasaki Disease during  
892 COVID-19 Pandemic. *Indian J Pediatr* **87**, 745-747 (2020).
- 893 6. Cheung, E., *et al.* Multisystem Inflammatory Syndrome Related to COVID-19 in  
894 Previously Healthy Children and Adolescents in New York City. *JAMA Volume*  
895 **324, Number 3**(2020).
- 896 7. Verdoni, L., *et al.* An outbreak of severe Kawasaki-like disease at the Italian  
897 epicentre of the SARS-CoV-2 epidemic: an observational cohort study. *Lancet*  
898 (2020).
- 899 8. Toubiana, J., *et al.* Kawasaki-like multisystem inflammatory syndrome in children  
900 during the covid-19 pandemic in Paris, France: prospective observational study.  
901 *BMJ* **369**, m2094 (2020).
- 902 9. Klocperk, A., *et al.* Case Report: Systemic Inflammatory Response and Fast  
903 Recovery in a Pediatric Patient With COVID-19. *Front Immunol* **11**, 1665 (2020).
- 904 10. Rowley, A.H. Understanding SARS-CoV-2-related multisystem inflammatory  
905 syndrome in children. *Nat Rev Immunol* **20**, 453-454 (2020).
- 906 11. Carter, M.J., *et al.* Peripheral immunophenotypes in children with multisystem  
907 inflammatory syndrome associated with SARS-CoV-2 infection. *Nat Med* (2020).
- 908 12. Gruber, C., *et al.* Mapping Systemic Inflammation and Antibody Responses in  
909 Multisystem Inflammatory Syndrome in Children (MIS-C). *Cell* (2020).
- 910 13. Consiglio, C., *et al.* The Immunology of Multisystem Inflammatory Syndrome in  
911 Children with COVID-19. *Cell* (2020).
- 912 14. Diorio, C., *et al.* Multisystem Inflammatory Syndrome in Children and COVID-19  
913 are distinct presentations of SARS-CoV-2. *J Clin Invest* (2020).
- 914 15. Leung, D.Y., Collins, T., Lapierre, L.A., Geha, R.S. & Pober, J.S. Immunoglobulin  
915 M antibodies present in the acute phase of Kawasaki syndrome lyse cultured  
916 vascular endothelial cells stimulated by gamma interferon. *J Clin Invest* **77**, 1428-  
917 1435 (1986).
- 918 16. Leung, D.Y., *et al.* Endothelial cell activation and high interleukin-1 secretion in  
919 the pathogenesis of acute Kawasaki disease. *Lancet* **2**, 1298-1302 (1989).
- 920 17. Leung, D.Y., *et al.* Endothelial activation in the pathogenesis of Kawasaki  
921 disease. *Transactions of the Association of American Physicians* **102**, 131-138  
922 (1989).
- 923 18. Leung, D.Y., *et al.* Two monokines, interleukin 1 and tumor necrosis factor,  
924 render cultured vascular endothelial cells susceptible to lysis by antibodies

- 925 circulating during Kawasaki syndrome. *The Journal of experimental medicine*  
926 **164**, 1958-1972 (1986).
- 927 19. Unterman, A., *et al.* Single-Cell Omics Reveals Dyssynchrony of the Innate and  
928 Adaptive Immune System in Progressive COVID-19. *medRxiv* (2020).
- 929 20. Mimitou, E.P., *et al.* Multiplexed detection of proteins, transcriptomes, clonotypes  
930 and CRISPR perturbations in single cells. *Nat Methods* **16**, 409-412 (2019).
- 931 21. Lydon, E.C., *et al.* Validation of a host response test to distinguish bacterial and  
932 viral respiratory infection. *EBioMedicine* **48**, 453-461 (2019).
- 933 22. Bertheloot, D. & Latz, E. HMGB1, IL-1alpha, IL-33 and S100 proteins: dual-  
934 function alarmins. *Cell Mol Immunol* **14**, 43-64 (2017).
- 935 23. Wilk, A.J., *et al.* A single-cell atlas of the peripheral immune response in patients  
936 with severe COVID-19. *Nat Med* **26**, 1070-1076 (2020).
- 937 24. Coperchini, F., Chiovato, L., Croce, L., Magri, F. & Rotondi, M. The cytokine  
938 storm in COVID-19: An overview of the involvement of the  
939 chemokine/chemokine-receptor system. *Cytokine Growth Factor Rev* **53**, 25-32  
940 (2020).
- 941 25. Lee, E.Y., Lee, Z.H. & Song, Y.W. CXCL10 and autoimmune diseases.  
942 *Autoimmun Rev* **8**, 379-383 (2009).
- 943 26. Dorothee Grumann, *et al.* Immune Cell Activation by Enterotoxin Gene Cluster  
944 (egc)-Encoded and Non-egc Superantigens from *Staphylococcus aureus*. *The*  
945 *Journal of Immunology* **181**, 5054-5061 (2008).
- 946 27. Habtezion, A., Nguyen, L.P., Hadeiba, H. & Butcher, E.C. Leukocyte Trafficking  
947 to the Small Intestine and Colon. *Gastroenterology* **150**, 340-354 (2016).
- 948 28. Hoyer, B.F., *et al.* Short-lived plasmablasts and long-lived plasma cells contribute  
949 to chronic humoral autoimmunity in NZB/W mice. *The Journal of experimental*  
950 *medicine* **199**, 1577-1584 (2004).
- 951 29. Kaneko, N., *et al.* Loss of Bcl-6-Expressing T Follicular Helper Cells and  
952 Germinal Centers in COVID-19. *Cell* **183**, 143-157 e113 (2020).
- 953 30. Rao, D.A., *et al.* Pathologically expanded peripheral T helper cell subset drives B  
954 cells in rheumatoid arthritis. *Nature* **542**, 110-114 (2017).
- 955 31. Ley, K. & Kansas, G.S. Selectins in T-cell recruitment to non-lymphoid tissues  
956 and sites of inflammation. *Nat Rev Immunol* **4**, 325-335 (2004).
- 957 32. Hildebrand, D., *et al.* Granzyme A produces bioactive IL-1beta through a  
958 nonapoptotic inflammasome-independent pathway. *Cell Rep* **9**, 910-917 (2014).
- 959 33. Zhou, Z., *et al.* Granzyme A from cytotoxic lymphocytes cleaves GSDMB to  
960 trigger pyroptosis in target cells. *Science* **368**, eaaz7548 (2020).
- 961 34. Franco, L.M., *et al.* Immune regulation by glucocorticoids can be linked to cell  
962 type-dependent transcriptional responses. *The Journal of experimental medicine*  
963 **216**, 384-406 (2019).
- 964 35. Stuart, T., *et al.* Comprehensive Integration of Single-Cell Data. *Cell* **177**, 1888-  
965 1902 e1821 (2019).
- 966 36. R Core Team. R: A language and environment for statistical computing. (R  
967 Foundation for Statistical Computing, Vienna, Austria, 2020).
- 968 37. Wickham, H. *ggplot2: Elegant Graphics for Data Analysis.* , (Springer-Verlag,  
969 New York, 2016).

- 970 38. Raredon, M.S.B., *et al.* Single-cell connectomic analysis of adult mammalian  
971 lungs. *Science Advances* **5**(2019).
- 972 39. Young, L.S., Arrand, J.R. & Murray, P.G. EBV gene expression and regulation. in  
973 *Human Herpesviruses: Biology, Therapy, and Immunoprophylaxis* (eds. Arvin, A.,  
974 *et al.*) (Cambridge, 2007).
- 975 40. Balazs, Z., *et al.* Long-Read Sequencing of Human Cytomegalovirus  
976 Transcriptome Reveals RNA Isoforms Carrying Distinct Coding Potentials. *Sci*  
977 *Rep* **7**, 15989 (2017).
- 978 41. Tirosh, I., *et al.* Dissecting the multicellular ecosystem of metastatic melanoma  
979 by single-cell RNA-seq. *Science* **352**, 189-196 (2016).
- 980 42. Chen, E.Y., *et al.* Enrichr: interactive and collaborative HTML5 gene list  
981 enrichment analysis tool. *BMC Bioinformatics* **14**, 128 (2013).
- 982 43. Kuleshov, M.V., *et al.* Enrichr: a comprehensive gene set enrichment analysis  
983 web server 2016 update. *Nucleic Acids Res* **44**, W90-97 (2016).
- 984 44. Giudicelli, V., Chaume, D. & Lefranc, M.P. IMGT/GENE-DB: a comprehensive  
985 database for human and mouse immunoglobulin and T cell receptor genes.  
986 *Nucleic Acids Res* **33**, D256-261 (2005).
- 987 45. Ye, J., Ma, N., Madden, T.L. & Ostell, J.M. IgBLAST: an immunoglobulin variable  
988 domain sequence analysis tool. *Nucleic Acids Res* **41**, W34-40 (2013).
- 989 46. Gupta, N.T., *et al.* Change-O: a toolkit for analyzing large-scale B cell  
990 immunoglobulin repertoire sequencing data. *Bioinformatics* **31**, 3356-3358  
991 (2015).
- 992 47. Gupta, N.T., *et al.* Hierarchical Clustering Can Identify B Cell Clones with High  
993 Confidence in Ig Repertoire Sequencing Data. *J Immunol* **198**, 2489-2499  
994 (2017).
- 995 48. Nielsen, S.C.A., *et al.* Human B Cell Clonal Expansion and Convergent Antibody  
996 Responses to SARS-CoV-2. *Cell Host Microbe* (2020).
- 997 49. Benjamini, Y. & Hochberg, Y. Controlling the False Discovery Rate - a Practical  
998 and Powerful Approach to Multiple Testing. *J R Stat Soc B* **57**, 289-300 (1995).
- 999